

1 A revised estimate of early Pliocene global mean sea level using geodynamic models of the
2 Patagonian slab window

3
4 Andrew Hollyday¹, Jacqueline Austermann¹, Andrew Lloyd¹, Mark Hoggard², Fred Richards³,
5 Alessio Rovere⁴

6
7 ¹Columbia University & Lamont-Doherty Earth Observatory

8 ²Australian National University

9 ³Imperial College London

10 ⁴MARUM & University of Bremen

11
12 Corresponding author: Andrew Hollyday (andrewh@ldeo.columbia.edu)

13
14 **Key Points:**

- 15 • Mantle flow through the Patagonian slab window, coupled with slab ponding in the
16 mantle transition zone, has uplifted eastern Patagonia since 5 Ma.
- 17 • Accounting for the effects of solid Earth deformation through time, global mean sea level
18 was 17.5 ± 6.4 m (1σ) in the early Pliocene.
- 19 • We present two sets of GIA models for Pliocene and modern disequilibrium as well as 18
20 5-Myr time-dependent mantle convection simulations.

21
22 **Abstract**

23
24 Paleo shorelines serve as measures of ancient sea level and ice volume but are affected by solid
25 Earth deformation including processes such as glacial isostatic adjustment (GIA) and mantle
26 dynamic topography (DT). The early Pliocene is an important target for sea-level reconstructions
27 as it contains information about the stability of ice sheets during a climate warmer than today.
28 Along the southeastern passive margin of Argentina, three paleo shorelines date to the early
29 Pliocene (4.8 – 5.5 Ma), and their variable present-day elevations (36 to 180 m) reflect a unique
30 topographic deformation signature. We use a mantle convection model to back-advect present-
31 day buoyancy variations in the Earth's mantle including those that correspond to the Patagonian
32 slab window. Varying the viscosity and initial tomography-derived mantle buoyancy structures
33 allows us to compute a suite of predictions of DT change that when compared to GIA-corrected
34 shoreline elevations allows us to identify both the most likely convection parameters and the
35 most likely DT change. Our simulations illuminate an interplay of upwelling asthenosphere
36 through the Patagonian slab window and coincident downwelling of the subducted Nazca slab in
37 the mantle transition zone. This flow leads to differential upwarping of the southern Patagonian
38 foreland since the early Pliocene in line with the observations. Using our most likely DT change
39 leads to an estimate of global mean sea level of 17.5 ± 6.4 m (1σ) in the early Pliocene. This
40 confirms that sea level was significantly higher than present and can be used to calibrate ice
41 sheet models.

42
43 **Plain Language Summary**

44

45 Understanding the height of global mean sea level during the early Pliocene, when
46 Earth's climate was warmer than today, will help to improve predictive models of current sea-
47 level rise. In eastern Patagonia, shorelines that formed during this time period have been
48 uplifted due to convective flow in the mantle beneath southern South America. We model both
49 mantle flow and the effects of ice sheet loading changes, which also cause Earth's topography to
50 evolve through time, to correct the present-day elevations of these shorelines. After subtracting
51 out the effects of solid Earth deformation, we calculate a global mean sea level of 17.5 ± 6.4 m
52 (1σ) in the early Pliocene.

53

54 1. Introduction

55

56 One billion people currently live less than 10 m above sea level (Kulp & Strauss, 2019). As
57 anthropogenic warming continues to melt continental ice and deliver it to the global oceans,
58 mitigation plans will require more confident predictions of sea-level rise. The capability of
59 coupled ice sheet-climate models to predict the amplitude and timing of sea-level rise during this
60 century relies on uncertain calibrations of ice sheet sensitivity to variable amounts of warming in
61 Earth's past (DeConto et al., 2021; DeConto & Pollard, 2016; Fischer et al., 2018). Past warm
62 intervals that are considered potential analogues for present and future climatic conditions
63 include late Pleistocene interglacials and the mid-Pliocene. These have been the focus of sea-
64 level reconstructions since they provide insight into how the planet may respond to future
65 anthropogenic warming (Burke et al., 2018; Dutton et al., 2015; Kopp et al., 2009). The early
66 Pliocene (5.3 to 3.6 Ma) is the warmest of these time periods with interglacial global mean
67 temperatures around 4°C higher than today and CO₂ concentrations above 400 ppm (Burke et
68 al., 2018; Collins et al., 2013; Fedorov et al., 2013; Haywood et al., 2013; Pagani et al., 2010).
69 Given rising temperature predictions for Earth's future, this time period serves as an increasingly
70 important calibration target for ice sheet models. In addition, sea-level constraints from the
71 Pliocene may inform the need to invoke controversial mechanics within ice sheet models (Pollard
72 et al., 2015).

73

74 Past approaches to estimate paleo sea level during the Pliocene and other warm periods
75 have relied on $\delta^{18}\text{O}$ in benthic foraminifera and Mg/Ca ocean paleo-temperature corrections;
76 however, effects such as carbonate diagenesis and unconstrained sea water chemistry and
77 salinity have led to high levels of uncertainty, precluding consensus on ancient sea levels (Raymo
78 et al., 2018; Rohling et al., 2014; Waelbroeck et al., 2002). Alternatively, mapping of paleo
79 shorelines provides a direct measure of past sea level and has generated relative sea level (RSL)
80 records that complement $\delta^{18}\text{O}$ -Mg/Ca paired methodologies (Rovere et al., 2014). However, due
81 to processes such as tectonic deformation, local sediment loading, glacial isostatic adjustment
82 (GIA), and mantle dynamic topography (DT), RSL records must be corrected for topographic
83 changes in elevation since their deposition that cause local sea level to diverge from the global
84 mean. To date, understanding and modeling these processes poses the biggest difficulty in
85 reliably inferring global mean sea level (GMSL) during the Pliocene. The work presented here is
86 among the first (Moucha & Ruetenik, 2017) to leverage variable uplift of Pliocene shorelines to
87 constrain mantle flow, correct shoreline elevations for deformation due to DT, and use this
modeling to infer GMSL.

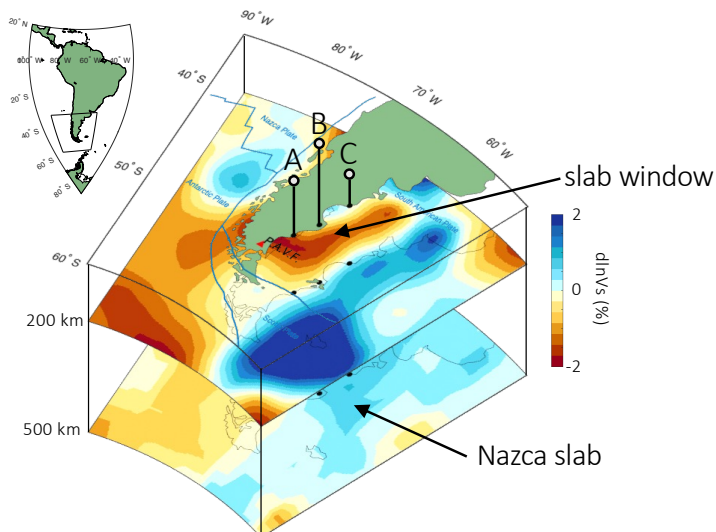
GIA describes the viscoelastic response of the solid Earth, its gravity field, and rotation axis to changes in ice and ocean loading. Raymo et al. (2011) examined its influence on Pliocene shorelines and found that GIA can cause changes in the far field of ice sheets of up to ~10 m. This contribution emphasized the need to correct for GIA when inferring past GMSL from Pliocene shorelines. In addition to GIA, convection in Earth's interior driven by density variations causes vertical deflections of Earth's surface and the geoid through time in what is termed DT (Hoggard et al., 2021). DT changes have been shown to significantly deform paleo shorelines: Moucha et al. (2008) used 3-D spherical shell convection models constrained by seismic tomography to demonstrate that even passive margins can experience significant DT change on the order of >200 m over the past 30 Myrs. Focused on more recent deformation, Rowley et al. (2013) predicted changes in DT on the order of ~50 m spanning the last 3 Myrs and found that they correlate with elevation variations in the Orangeburg Scarp located along the U.S. East Coast. While Rowley et al. (2013) did not use their DT predictions to infer GMSL, Moucha & Ruetenik (2017) revisited deformation along the Orangeburg Scarp considering both mantle convection and sediment loading-driven topographic changes and estimated a GMSL of approximately 15 m in the mid-Pliocene. For even more recent timescales, the amplitude of DT change contamination is expected to diminish; however, Austermann et al. (2017) demonstrated that to constrain GMSL during the last interglacial (MIS 5e; ~122 ka) to meter-scale accuracy, a correction for DT change must also be performed. While the importance of correcting paleo shorelines for DT change across a range of timescales is now well-known, under-resolved mantle structure, and uncertain plate motion reconstructions and conversions from seismic wave speeds to mantle rheology, densities, temperatures, and viscosities often inhibit reliable corrections.

Paleo shorelines that date to the early Pliocene are sparse, and given the challenges in modeling their geodynamic deformation, it is difficult to use them to obtain reliable GMSL estimates from the early Pliocene. The most confident early Pliocene estimate to date comes from Mallorca, Spain, where a GMSL of 25.1 m (median, 10.6 – 28.3 m, 16th – 84th percentile uncertainty bounds) at 4.39 ± 0.39 Ma (2σ) Ma was inferred from phreatic overgrowth on speleothems (Dumitru et al., 2019). In addition, a recently dated early Pliocene sedimentary sequence from South Africa records a similar sea level range, but this datum was not originally corrected for GIA or DT change (Hearty et al., 2020). Rovere et al. (2020) corrected this RSL record for GIA and used the long-wavelength global convection models from Müller et al. (2018) to correct for DT change and estimate an early Pliocene GMSL of 23.4 ± 35.8 m (mean, 1σ). In Camarones, Argentina, Rovere et al. (2020) estimated GMSL of 28.4 ± 11.7 m (mean, 1σ) on the basis of a transgressive conglomerate unit containing preserved bivalve and gastropod fauna dated to 4.96 ± 0.27 Ma (2σ), which was corrected for GIA as well as DT change using continental scale models from Flament et al. (2015). In both the estimates from Argentina and South Africa, DT correction introduces significant uncertainty into their GMSL inference as the convection models were not tested against independent geodynamic observations from those regions.

In this study, we revisit the Camarones site in Argentina (Rovere et al., 2020) as well as two sites to the south (within 600 km) that also exhibit early Pliocene shoreline deposits (del Río et al., 2013) (Fig. 1, Table 1). The three Patagonian deposits consist of fossiliferous, coarse-grained sandstone and gravel beds containing fragmented species of *Chlamys actinodes*

(southern two localities; Cañadón Darwin and the Terrace of the Cerro Laciá) and cemented fine conglomerates with species from the Ostedidae family (northern locality; Camarones). These faunal assemblages have been sampled and analyzed, and their $^{87}\text{Sr}/^{86}\text{Sr}$ (Strontium Isotope Stratigraphy, SIS) ages fall in the interval from 5.33 – 4.69 Ma (2σ ; del Río et al., 2013; Rovere et al., 2020), slightly predating the earliest Pliocene sea level estimates from Mallorca and South Africa (Dumitru et al., 2019; Hearty et al., 2020). They occur at mean elevations of 70 ± 5 , 177.5 ± 7.5 , and 36.2 ± 2.7 m above sea level (south to north), along a near-longitudinal profile on the tectonically inactive passive margin of southern Argentina (Fig. 1). The elevation uncertainties stem from instrumental and mapping error as well as estimates for the water depth at which each species can grow (see del Río et al., 2013 & Rovere et al., 2020). Noting the comparatively long-wavelength spatial patterns expected for GIA (Raymo et al., 2011), we hypothesize these sites, which show a clear short-wavelength (<600 km) topographic signature, have been deformed by convective mantle flow.

145



146

147

Figure 1.

148

Schematic diagram of the Patagonian slab window. Sites A, B, and C correspond to uplifted sea level indicators that date to the early Pliocene. The upper mantle structure is imaged by the SL2013sv tomography model (Schaeffer & Lebedev, 2013), with slow seismic wave speeds at shallow depths (200 km). Transition zone structure (500 km) from the TX2011 tomography model (Grand et al., 2002) shows faster velocities that reflect the previously subducted Nazca slab. Sites A (Cañadón Darwin), B (Terrace of the Cerro Laciá), and C (Caramones) are occur at mean elevations of 70 ± 5 , 177.5 ± 7.5 , and 36.2 ± 2.7 m above sea level, respectively.

149

150

151

152

153

154

155

156

157

158

159

160

Geodynamic reconstructions indicate a complex history of ridge subduction within the South American subduction zone that has led to the generation and growth of a slab window beneath Patagonia (e.g., Breitsprecher & Thorkelson, 2009). By ~ 20 Ma the Nazca-Phoenix ridge reached its final phase of subduction beneath Patagonia, in which convergence along the Nazca-South American plate boundary and oblique convergence (left-lateral) strike-slip motion along

161 the Phoenix-South American plate boundary may have generated an early slab window beneath
 162 southernmost Patagonia. The intersection and subsequent subduction of the Nazca-Phoenix-
 163 Antarctic triple junction at the South American subduction zone at ~18 Ma set into motion a
 164 dramatic modification of the underlying mantle structure that triggered the formation or
 165 widening of a slab window. Much of this growth was accommodated by northward migration
 166 (~1,000 km) of the Nazca-Antarctic-South American triple junction, while slower growth
 167 occurred by southward migration of the Antarctic-Phoenix-South American triple junction until
 168 ~3.3 Ma when the Phoenix plate was captured by the Antarctic plate (Eagles, 2004; Livermore et
 169 al., 2000). Although subduction of the Antarctic plate between these two triple junctions began
 170 at ~17 Ma, models suggest slow convergence rates and that the Antarctic slab may have only
 171 reached ~45 km depth (Breitsprecher & Thorkelson, 2009).

172

Table 1

*Locations, measured elevations, ages, and geodynamic corrections for the three paleo-shorelines
 in eastern Patagonia.*

	Site A (southernmost; del Río et al., 2013)	Site B (middle; del Río et al., 2013)	Site C (northernmost; Rovere et al., 2020)
Latitude (°)	-49.628	-47.629	-44.790
Longitude (°)	-67.715	-66.392	-65.728
Elevation (m; 1σ)	70.0 ± 5.0	177.5 ± 7.5	36.2 ± 2.7
Age (Ma; 2σ)	5.15 ± 0.18	5.10 ± 0.21	4.96 ± 0.27
GIA correction (m; 1σ)	-10.4 ± 2.8	-10.5 ± 2.7	-11.4 ± 2.8
DT correction (m)	66.2	154.7	32.4

173

174 In turn, the geodynamic evolution of the Patagonian slab window has led to regional
 175 volcanism. Anhydrous sub-slab Plio-Quaternary lavas with Ocean Island Basalt affinities have
 176 subsequently erupted across southern Patagonia delineating approximate boundaries of the slab
 177 window (e.g., Gorring et al., 2003; Guivel et al., 2006), and the subsurface slab window geometry
 178 has been revealed by a recent adjoint seismic tomographic inversion (Fig. 1; Lloyd et al., 2020).
 179 The hot upwelling asthenosphere through the Patagonian slab window and coincident
 180 downwelling of the underlying, remnant Nazca slab is a probable setting for changes in DT
 181 through time that could explain differential upwarping of the three observed early Pliocene
 182 paleo shorelines.

183 Here, we present mantle convection models constrained by inferences of the mantle's
 184 density structure from global seismic tomography along with GIA modeling to better understand
 185 how the three early Pliocene sea-level deposits were subsequently deformed. We use the
 186 differential elevations of the three early Pliocene sea-level indicators to investigate slab window
 187 subduction behavior and constrain Earth structure. We further combine results from DT and GIA
 188 modeling to correct the three RSL records for post-depositional effects and infer GMSL from the
 189 early Pliocene.

190

191 2. Methods

192
193
194
195
196
197
198
199
200

With the goal of computing an early Pliocene GMSL, we reassess the deformational history of published sea-level deposits by (1) correcting the observed elevations of the shorelines for GIA (section 2.1), (2) modeling a suite of mantle convection simulations that reproduce the dynamic behavior of the Patagonian slab window and short-wavelength DT patterns (section 2.2), and (3) leveraging the different elevations of the shorelines, residual topography observations from the surrounding oceanic basins, and the early Pliocene sea level observation from Mallorca to perform data-model comparison and constrain otherwise highly uncertain solutions of DT change (section 2.3).

201

202 **2.1 GIA correction**

To determine the contribution of GIA to deformation of the shorelines, we solve the gravitationally self-consistent sea-level equation for a depth dependent Maxwell viscoelastic Earth structure (Kendall et al., 2005). Our approach accounts for shoreline migration and the feedback of load changes into Earth's rotation axis. Following the approach described in Raymo et al. (2011) and Dumitru et al. (2019), we deconstruct the GIA signal into two parts: (1) the ongoing response to the last glacial cycle and (2) the response to ice sheet variability during the early Pliocene. We use a spherically symmetric elastic and density structure from the seismic reference model PREM (Dziewonski & Anderson, 1981). For the depth dependent viscosity structure, we combine two lithospheric thicknesses (71 km and 96 km) with two upper mantle viscosities (3×10^{20} Pa s, 5×10^{20} Pa s) and six lower mantle viscosities (3×10^{21} Pa s, 5×10^{21} Pa s, 7×10^{21} Pa s, 1×10^{22} Pa s, 2×10^{22} Pa s), generating a total of 24 different radial Earth structures. The transition from upper to lower mantle is defined at 670 km depth. While radial viscosity profiles neglect known lateral variations revealed by seismic tomography (e.g., Ritsema et al., 2011; Russo et al., 2022), employing a range of estimates of mantle viscosity allows us to estimate the uncertainty introduced by this assumed 1-D structure.

For the first correction, we use an extension of the ICE-6G_C ice history which prescribes global ice extents from 122 ka to present-day (Peltier et al., 2015; Peltier & Fairbanks, 2006). We then allow our models to evolve past the present day until they reach steady-state isostasy, which enables us to estimate how much present-day shorelines are affected by the last glacial cycle. For the second correction, we account for GIA associated with excess melt during the Pliocene when ice sheets were smaller than today. With the same suite of radial Earth structures used for the first correction, we pair an ice history that varies Antarctic and—to a much smaller degree—Greenland ice volume following the LR04 benthic isotope stack (Lisiecki & Raymo, 2005). We use an ice reconstruction for Antarctica that is based on Pollard et al. (2015), who modeled the Antarctic ice sheet during the mid-Pliocene. This reconstruction, which consists of 41 m of sea level equivalent ice, represents an intermediate ice distribution characterized by major deglaciation of the West Antarctic Ice sheet (WAIS) and notable retreat from Wilkes Basin, Aurora Basin, and the Recovery Ice Stream (Cook et al., 2013; Naish et al., 2009; Pollard et al., 2015; Scherer et al., 2016). For the ice distribution in Greenland, we assume 50 cm of sea level equivalent ice stored along the eastern coast since this high terrain was likely the first to glaciate (Bierman et al., 2016). We then scale the ice height for this model uniformly up and down following the LR04 benthic isotope stack (Lisiecki & Raymo, 2005), which is scaled

235 to GMSL using a conversion factor of 0.033 ‰ m⁻¹. This conversion was chosen to yield a GMSL
236 during the early Pliocene that is consistent with our final result (and was found through
237 iteration). Since the exact interglacial that the early Pliocene the shorelines formed during is
238 unknown, we take the GIA correction at seven possible interglacials that are consistent with the
239 age uncertainties of the three shorelines (5.235, 5.135, 5.090, 5.020, 4.925, 4.874, and 4.825
240 Ma). Our reconstruction, used in our GIA models, yields early Pliocene GMSL ranging from 13.8
241 to 21.3 meters during the 7 interglacials. We note that GMSL is calculated as ice equivalent sea
242 level assuming a fixed ocean area (see Dumitru et al., 2019). Finally, we combine the two GIA
243 components, with respective radial Earth structures, to generate 168 different predictions (24
244 Earth structures × 7 interglacial ages) of deformation due to GIA.

245

246 2.2 Mantle convection simulations

247 We perform a suite of mantle convection simulations to discern the effects of changes in
248 DT on the deformational history of the three early Pliocene paleo shorelines. To model
249 convection we use the finite element convection code ASPECT, which solves the governing
250 equations for mantle convection: conservation of mass, energy, and momentum employing
251 state-of-the-art numerical methods (Bangerth et al., 2020; Heister et al., 2017; Kronbichler et al.,
252 2012). We use ASPECT 2.2.0 to run global incompressible back-advection simulations for the
253 mantle, which reverse flow through time, with free-slip boundary velocity conditions and
254 thermal boundary conditions consistent with surface and core-mantle-boundary (CMB)
255 temperatures (0°C and 3027°C, respectively). We assign values for reference temperature
256 (1333°C), reference density (3300 kg m⁻³), and specific heat (1250 J K⁻¹ kg⁻¹). Thermal diffusivity
257 is set to zero since diffusion is not a time-reversible process and would be minimal over a 5 Myr
258 timespan. Radially-varying gravity and thermal expansivity profiles are adopted from Glišović &
259 Forte (2015). We pair 3 different viscosity models with 6 different temperature structures of the
260 mantle resulting in a total of 18 time-dependent simulations.

261 The initial temperature structures of our mantle convection models are derived from
262 seismic tomography. We use several tomographic models of shear wave speed and employ a
263 different conversion from wave speed to temperature for the upper mantle (0 – 410 km) than
264 the transition zone and lower mantle (410 km – CMB) since our upper mantle conversion
265 method is only applicable to an olivine-dominated composition. All temperature models include
266 a section of linearly merged temperatures between 300 km and 400 km to prevent
267 discontinuous jumps in the converted temperature models. The full conversion scheme from
268 seismic velocities to temperatures in the upper mantle, transition zone, and lower mantle is
269 illustrated in Supplementary Figure 1.

270 Upper mantle temperature is derived from two higher resolution velocity models: GLAD-
271 M25 and SL2013sv (Lei et al., 2020; Schaeffer & Lebedev, 2013). As a note, SL2013sv was
272 generated using only shorter period surface wave data, while GLAD-M25 also used body wave
273 data. We convert to temperatures using an experimentally-derived relation describing the
274 anelastic properties of the mantle analogue material, borneol, calibrated with geophysical
275 observations (Richards et al., 2020; Yamauchi & Takei, 2016). Calibration targets are oceanic
276 lithospheric temperatures, the radial attenuation structure of the upper mantle (Dalton et al.,
277 2009), and the bulk upper mantle viscosity. We further require the average computed
278 temperatures at each depth to be consistent with a 1333°C reference temperature (Richards et

279 al., 2020). The calibrated parameterization, which is based on tomography model-specific
 280 inversions of the seven free parameters of the Yamauchi & Takei (2016) relation (parameters
 281 reported in Sup. Table 1), describes the full temperature domain of the velocity-to-temperature
 282 relationship including the high temperature segment, where using a purely anharmonic relation
 283 would lead to over-prediction of temperatures owing to the significant effects of anelastic
 284 deformation in the upper mantle (Richards et al., 2020). Within the continental lithosphere,
 285 temperatures converted from seismic velocities are highly uncertain due to compositional
 286 differences between the sublithospheric mantle and the continental lithosphere. Following
 287 Jordan (1978), we assume that continents are neutrally buoyant and therefore set, at each
 288 depth, the temperature within the continental lithosphere equal to the mean temperature
 289 outside of continents (as in Richards et al., 2020). Changes in temperature and thickness of the
 290 oceanic lithosphere leads to a significant topographic signal due to isostasy. This signal and its
 291 resulting change through time is sometimes but not always included in the definition and
 292 modeling of DT (Forte et al., 1993; Hoggard et al., 2021). Here we treat the oceanic lithosphere
 293 as neutrally buoyant (i.e., set the temperature to follow the same depth profile as within the
 294 continents) since changes in DT driven by ocean lithosphere cooling are expected to be minimal
 295 in the Argentine Abyssal Plain, which evolved to full sea-floor spreading in mid-Cretaceous times.
 296 We perform an independent assessment of the tomography-based temperature models by
 297 comparing them to the equilibration pressures and temperatures of mantle xenoliths (Sup. Table
 298 2) erupted from the Pali-Aike Volcanic Field in southern Patagonia (Wang et al., 2008). These
 299 thermobarometry calculations use measured major element compositions from olivine,
 300 orthopyroxene, clinopyroxene, and garnet that are hosted in high-temperature (> 900 °C)
 301 peridotites, garnet-spinel harzburgites, and garnet Iherzolites dated to the Plio-Quaternary
 302 (Bhanot et al., 2020; Nickel & Green, 1985; Taylor, 1998; Wang et al., 2008).

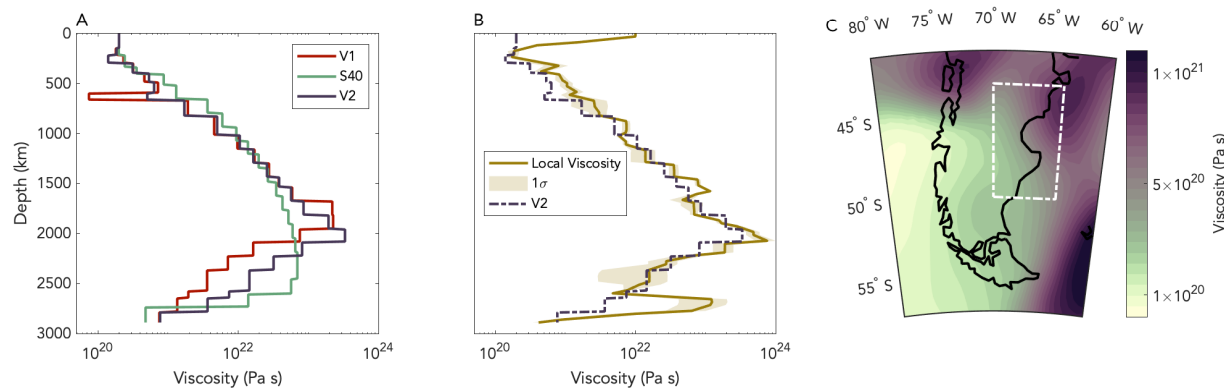
303 Structure in the lower mantle and transition zone (below 400 km) is obtained from three
 304 lower resolution, global tomography models: TX2011, S362ANI+M, and S40RTS (Grand et al.,
 305 2002; Moulik & Ekström, 2014; Ritsema et al., 2011). We convert relative seismic wave velocities
 306 to relative densities using a simple anharmonic scaling with a depth-varying conversion factor
 307 from Steinberger (2016). We use a linearly interpolated depth-varying thermal expansion profile
 308 based on Glišović & Forte (2015) to convert density perturbations to relative temperatures. We
 309 assign reference values that are consistent with the convection parameters detailed above.

310 Viscosity is assumed to vary radially and laterally. We use 3 radial viscosity profiles that
 311 come from inversions of GIA and convection observables (Fig. 2A; Forte et al., 2010; Mitrovica &
 312 Forte, 2004; Steinberger, 2016). To enforce a more rigid lithosphere while limiting sharp
 313 viscosity contrast that otherwise causes shallow small-scale convection and model artifacts in
 314 our DT predictions, we first set all radial profiles to 2×10^{20} Pa s above 150 km, then assign a
 315 constant viscosity of 1×10^{22} Pa s above the lithosphere-asthenosphere boundary (LAB), which is
 316 defined as the 1200°C isotherm specific to each temperature model (described below). We
 317 lastly assign a viscosity of 5×10^{21} Pa s between the LAB and 120% of its depth to smooth vertical
 318 viscosity variations. Lateral variability is introduced through an Arrhenius relationship:
 319

$$320 \eta(z, T) = \eta_r(z) e^{\frac{-A(T-T_r)}{T_r}}, \quad (1)$$

321

322 where $\eta(z, T)$ is the mantle viscosity that varies with both depth, z , and the laterally variable
 323 temperature, T , $\eta_r(z)$ is the radial reference viscosity, T_r is the reference incompressible
 324 temperature set to 1333°C, and A is a thermal viscosity exponent set to 0.01 (Fig. 2B,C; see
 325 Bangerth et al., 2020 p.163 for details). As a note, viscosity remains constant at depths $\leq 120\%$ of
 326 the LAB and is not scaled laterally by temperature as is the case through the remainder of the
 327 mantle.
 328



329
 330
 331
Figure 2.

332 A: Radial viscosity profiles used in the mantle convection suite. As a note, these profiles are set to 2×10^{20} Pa s.
 333 These profiles are scaled laterally according to the different 3D tomography-derived mantle temperature models. B: Local depth-averaged viscosity structure from within the white rectangle (shown on the map in C) from a best-fitting
 334 convection model that uses the laterally-scaled V2 radial profile. Associated 1σ viscosity variations are shown in the
 335 shaded tan envelope. C: A map of lateral viscosity variations at 300 km depth. Model shown in B & C is from
 336 SL2013sv upper mantle and TX2011 transition zone and lower mantle structure (Grand et al., 2002; Schaeffer &
 337 Lebedev, 2013).
 338

339 DT is calculated from radial stresses at the surface and the density contrast between the
 340 crust and the overlying material (Zhong et al., 1993). We take into account that the overburden
 341 changes from air to water along the shorelines following the method outlined in Austermann &
 342 Mitrovica (2015), using a 90 km-thick lithosphere. Convection-caused perturbations to the geoid
 343 are also accounted for and included in the final calculation of change in DT since we are
 344 interested in sea-level changes rather than just solid Earth deformation. Our convection
 345 simulations back-advect the present-day mantle structure for 5 Myrs and calculate DT and geoid
 346 anomalies at each timestep (geoid changes are included in our use of “DT changes” for the
 347 remainder of the manuscript). Our calculations are incompressible and do not include phase
 348 changes, thermal boundary layers (except at the surface and CMB), internal radiogenic heat
 349 production, or deflection of internal boundaries within the simulations; however, the initial
 350 temperature structures we prescribe implicitly include some of these important dynamics.
 351 While we do not model brittle deformation in the crust within our simulations, the absence of
 352 mapped neotectonic structures (e.g., faulting) in this region indicates minimal crustal
 353 deformation has occurred since the Pliocene (Perucca et al., 2016).

354 To calculate the change in DT through time, we must take into account how the motion
 355 of tectonic plates has displaced DT fields over time (Hoggard et al., 2021). We do so by assuming
 356 plate motion that includes both rotating the global plates relative to each other in a no-net-

358 rotation reference frame from Argus et al. (2011) and applying a total lithospheric rotation of
 359 $0.25^\circ \text{ Ma}^{-1}$ right-handed about $57.1^\circ\text{S}, 68.6^\circ\text{E}$ from Zheng et al. (2014). We explore the total
 360 rotation uncertainty by also including results rotated by 1σ (0.195 and $0.305^\circ \text{ Ma}^{-1}$) and 2σ (0.14
 361 and $0.36^\circ \text{ Ma}^{-1}$) of their stated uncertainty.

362

363 2.3 Data-model comparison

364 We first correct the observed elevations, E , of the three early Pliocene shorelines for GIA
 365 by subtracting the mean GIA correction, \overline{GIA}_i , (averaged over different Earth structures and
 366 different interglacials) from the mean observed elevation of paleo sea level at each location, i .
 367 This yields the GIA-corrected elevation, \overline{GE}_i :

368

$$369 \quad \overline{GE}_i = \overline{E}_i - \overline{GIA}_i \quad (2)$$

370

371 and associated uncertainty, σ_{GE_i} :

372

$$373 \quad \sigma_{GE_i} = \sqrt{\sigma_{E_i}^2 + \sigma_{GIA_i}^2}, \quad (3)$$

374

375 where σ_{E_i} is the uncertainty in elevation measurements and indicative range or habitable water
 376 depth for the observed species (see del Río et al. (2013) and Rovere et al. (2020)) and σ_{GIA_i} is the
 377 uncertainty in the GIA correction due to variable Earth structure and ice loading. Rovere et al.
 378 (2020) incorporated an estimate for indicative range into their reported RSL elevation. While del
 379 Río et al. (2013) does not explicitly report this component of the elevation uncertainty, the
 380 elevation uncertainty remains conservative with at most 15 m (2σ).

381 Next, we compare the GIA-corrected elevations to our DT predictions. To do so we
 382 subtract the DT prediction, $DT_{i,m}$, where m specifies the DT model, from the GIA-corrected
 383 elevation (\overline{GE}_i) at each site to obtain a GMSL estimate for this site:

384

$$385 \quad GMSL_{i,m} = \overline{GE}_i - DT_{i,m} \quad (4)$$

386

387 We then calculate a GMSL as the weighted mean between the three sites, where weights are the
 388 squared inverse of the uncertainty in GIA-corrected elevation at each site:

389

$$390 \quad w_i = 1/\sigma_{GE_i}^2 \quad (5)$$

391

$$392 \quad GMSL_m = \frac{\sum_{i=1}^N (w_i \cdot GMSL_{i,m})}{\sum_{i=1}^N w_i}, \quad (6)$$

393

394 where N is the number of shorelines ($N = 3$). This is performed for each DT prediction, m , which
 395 in total consists of 90 predictions (i.e., 5 different total rotations for each of the 18 convection
 396 runs). As a note, we do not formally invoke the age uncertainty of the three shorelines when
 397 correcting for DT change. Instead, all DT corrections are based on simulations that ran for 5

398 Myrs, given the limited change in DT that would be expected over the relatively short time span
 399 associated with the age uncertainty of the shorelines.

400 In order to understand how well our DT model fits the spatial variability of the data, we
 401 finally calculate the mean squared weighted deviation (MSWD) for each DT model:

402

$$403 \quad MSWD_m = \frac{1}{N} \sum_{i=1}^N \left[\frac{(GMSL_{i,m} - GMSL_m)^2}{\sigma_{GE_i}^2} \right] \quad (7)$$

404

405 Given the limited spatial resolution of the tomography models, we don't limit the data-
 406 model comparison to only the exact location of the data but sample modeled DT predictions
 407 surrounding each site with a maximum distance of 140 km. This distance is comparable to the
 408 lateral resolution of our upper mantle tomography models. We then chose the smallest MSWD
 409 for each convection-plate rotation pair. A small MSWD signifies that the elevation pattern of the
 410 shoreline (i.e., their differential elevations) is matched well by the DT prediction. Specifically, an
 411 MSWD of 1 means that the DT prediction is on average 1σ away from the observation. Lastly,
 412 our GMSL uncertainty is computed by taking a weighted standard deviation:

413

$$414 \quad \sigma_{GMSL_m} = \sqrt{\frac{\sum_{i=1}^N w_i (GMSL_{i,m} - GMSL_m)^2}{\sum_{i=1}^N w_i}}, \quad (8)$$

415 where the weights are defined by equation 5.

416 In addition to leveraging the GIA-corrected elevations of the three Pliocene shorelines in
 417 Argentina, we also draw on additional constraints on present-day DT and bounds of GMSL to
 418 further narrow in on the most likely DT models. First, we reject DT models associated with GMSL
 419 predictions outside of a realistic range of 10 – 40 m in the early Pliocene; this range was
 420 conservatively chosen to encompass the wide uncertainty estimates for GMSL during this
 421 interval (e.g., Dumitru et al., 2019). Second, we compare our present-day DT predictions to 25
 422 local residual topography measurements and their reported uncertainties (Hoggard et al., 2017).
 423 For each DT prediction we calculate the MSWD (for fits to residual topography) and reject those
 424 that yield MSWDs greater than 20. Third, we compute GMSL in Mallorca, Spain, where
 425 analogous, well-mapped early Pliocene sea level indicators occur (Dumitru et al., 2019). We do
 426 so by subtracting our prediction of DT change from the GIA-corrected elevations. We only keep
 427 those convection simulations that predict GMSL that varies by less than 5 m from our estimate
 428 from Patagonia. We use the MSWDs that describe how well each convection run fits the
 429 deformation pattern in Argentina (equation 6) as well as these three additional criteria to
 430 identify successful rheological parameters and density structures, and calculate a best estimate
 431 of GMSL. We further explore the sensitivity of our best estimate of GMSL to the cutoff values
 432 chosen in each of the criteria.

433

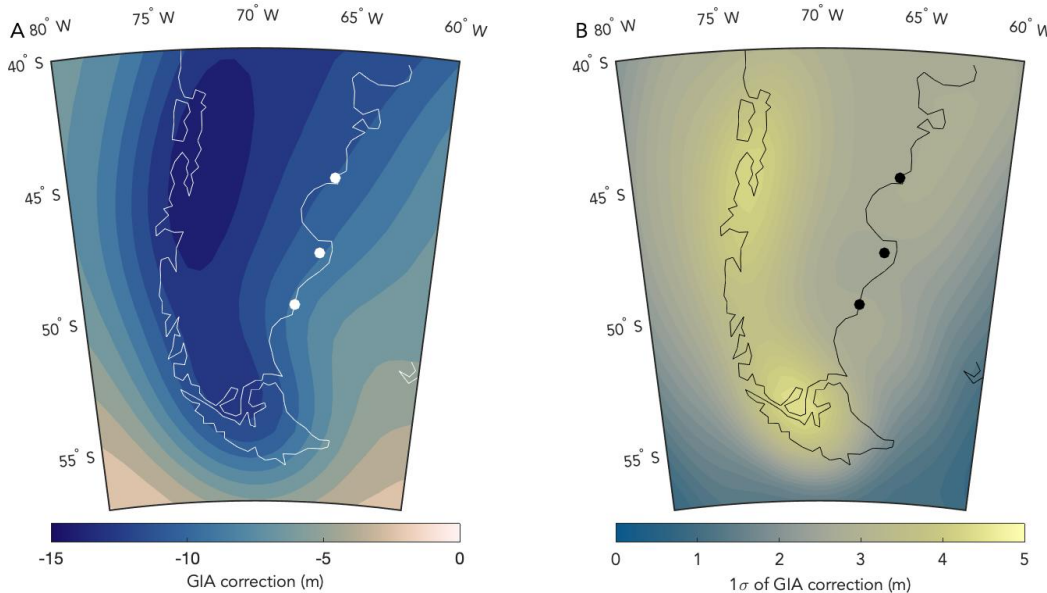
434 3. Results and discussion

435

436 3.1 GIA correction

437 Ongoing adjustment to ice changes over the last glacial cycle results in a GIA correction
 438 that is lowest (most negative) at the center of the Last Glacial Maximum (LGM) Patagonian ice
 439 sheet and increases away from it (Fig. 3A). This is caused by ice unloading in western Patagonia

440 and the associated solid Earth rebound, which diminishes with distance from the former ice load.
 441 In eastern Patagonia, this results in a GIA correction for the three paleo shorelines that varies
 442 from -10 to -5 m, which means that this region will continue to uplift by 5 to 10 meters until the
 443 solid Earth (and gravity field) has fully equilibrated to ice changes from the last glacial cycle.
 444



445
 446
 447
 448
 449 Figure 3.
 450
 451

452 GIA correction and uncertainty. A: Mean GIA correction for Patagonia from 168 different predictions (24 Earth
 453 structures \times 7 interglacials). B: 1σ uncertainty of the GIA correction.
 454

455 Ice sheet variability during the early Pliocene was predominantly driven by Antarctic ice
 456 change, which is associated with a fall in GMSL since the early Pliocene. The GIA correction
 457 associated with this overall ice change is largest in areas of former ice cover (Raymo et al., 2011).
 458 Patagonia is far enough away from these ice load changes that adjustment is very similar at each
 459 of the three shorelines resulting in a GIA correction that varies from -5 to -2 m. This correction
 460 means that local sea level was lower than GMSL due to differential loading of meltwater
 461 between oceans and continents (see Raymo et al. (2011) for a detailed discussion).

462 Combining the two GIA corrections yields values of -10.4 ± 2.8 m, -10.5 ± 2.7 m, and -11.4 ± 2.8 m (1σ) at the paleo shoreline locations from south to north (Fig. 3). The small
 463 differences between these estimates demonstrate that GIA alone cannot explain the large
 464 differences in the observed present-day elevations of the three paleo shorelines.
 465

466 3.2 Mantle flow simulations

467 3.2.1 Mantle temperature and viscosity

468 The geometry of the slab window varies across our temperature model suite due to
 469 differences in the tomographic models. Temperatures converted from both the SL2013sv and

469 GLAD-M25 models predict warm temperatures corresponding to the slab window that extend
470 over a broad north-south spatial range ($\sim 38^{\circ}\text{S}$ to 50°S), which is a larger extent than has been
471 imaged in the ANT-20 model, which is expected since ANT-20 is a full waveform, regional model
472 (Lloyd et al., 2020). Seismic wave speeds from ANT-20 were not converted to temperature as
473 this model has not yet been calibrated for our upper mantle conversion method. SL2013sv
474 results in warm temperatures that cross the Andes at the Chile Triple Junction (CTJ) and extend
475 north under the continent (Fig. 4A). Features in GLAD-M25 are similar but clearly broader and
476 might under-resolve local structure (Fig. 4B). The depth extent of relatively warm (above 1333°C
477 reference temperature) slab-window asthenosphere also varies by tomography model: SL2013sv
478 images inflowing asthenosphere that extends to approximately 250 km depth, while GLAD-M25
479 extends slightly deeper to approximately 300 km. Temperatures within the slab window peak
480 around $1370 - 1420^{\circ}\text{C}$ at 100 km depth (Fig. 4A,B). Our suite of temperature models agrees with
481 shallow (50 to 80 km) thermobarometric calculations of local pressures and temperatures from
482 Plio-Quaternary xenoliths erupted from the Pali-Aike Volcanic Field (Fig. 5). Our temperature
483 fields is also generally consistent with the WINTERC-G temperature model (Fullea et al., 2021),
484 which shows local incompressible temperatures around $\sim 1350 \pm 50^{\circ}\text{C}$ in the upper mantle. This
485 model, which inverted seismic waveforms, satellite gravity measurements, surface elevation, and
486 heat flow data using a self-consistent thermodynamic framework, shows a hot mantle anomaly
487 at 200 km depth that transitions to colder temperatures by 260 km. The slab geometry that has
488 been imaged in WINTERC-G is more similar to that of SL2013sv, compared to GLAD-M25, which
489 defines a more diffuse structure (Fullea et al., 2021). Further, An et al. (2015) have produced
490 temperature estimates beneath the Antarctic plate based on laboratory and seismological
491 constraints of anharmonicity and anelasticity of olivine using the conversion from Goes et al.
492 (2000), and their temperature estimates fall in the middle of our two estimates from SL2013sv
493 and GLAD-M25 in the overlapping regions, mostly under the Southern Ocean. Agreement
494 between these local and spatially continuous independent estimates of mantle temperatures
495 provides support for the seismic velocity-to-temperature conversion methodology in the shallow
496 mantle. The subducted Nazca slab resides at around 450 km with cooler temperatures, varying
497 from $1175 - 1250^{\circ}\text{C}$ (Fig. 4C,D). In the lower mantle, local structure consists of two dominant
498 regions ($\sim 660 - 1800$ km and $\sim 1800 - 2900$ km) of relatively warm and cold temperatures,
499 respectively (Fig. 4C,D). In general, temperature models mapped from the TX2011 tomography
500 model in the lower mantle reflect the shortest wavelength temperature variability, while those
501 derived from S362ANI+M show broad long wavelength structure; S40RTS-derived models
502 represent an intermediate wavelength structure in the lower mantle.

503 Our temperature fields lead to viscosity variations of ± 1 order of magnitude from our
504 reference profiles (Fig. 2B,C). Within the slab window we compute lowest viscosities of 3×10^{20}
505 to 4×10^{20} Pa s at 300 km depth. We compute higher viscosities in the transition zone (at 450
506 km depth) of $4 \times 10^{21} - 5 \times 10^{21}$ Pa s (Fig. 2B). These viscosity variations possibly underestimate
507 the true variability but this smaller variability was chosen to ease numerical convergence and
508 computation time.

509

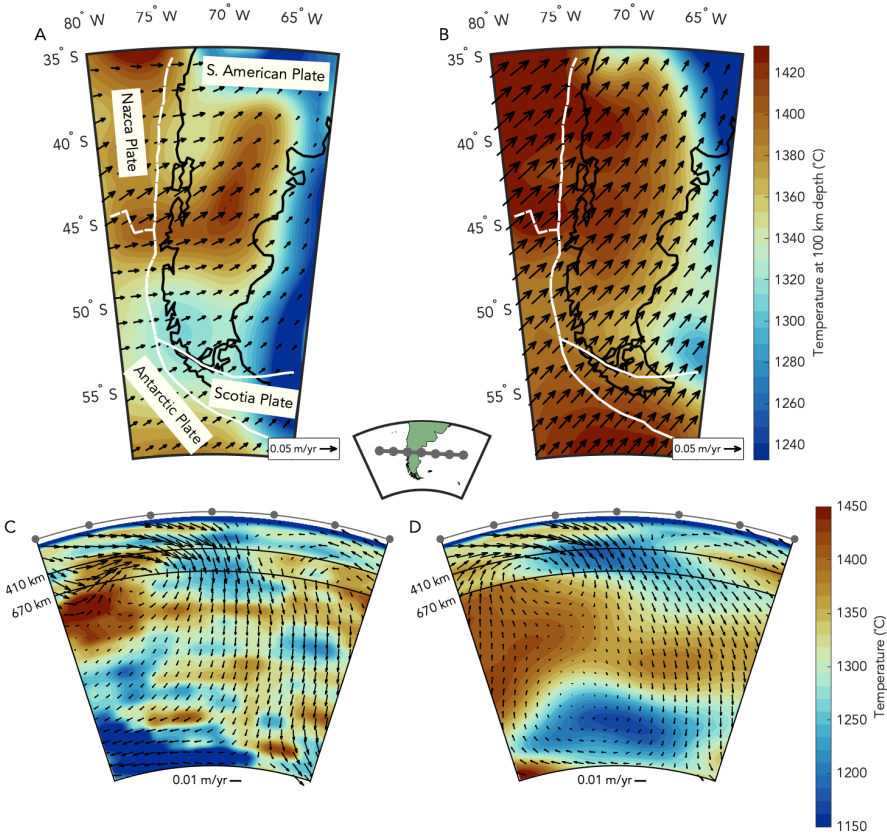


Figure 4.

510
511
512
513
514
515
516
517
518
519
520
521

Present-day flow predictions showing inflow of asthenosphere from beneath the Antarctic plate into the Patagonian slab window. A: Planview mantle flow at 100 km depth initialized with a temperature model computed from the SL2013sv tomography model (Schaeffer & Lebedev, 2013) in the upper mantle. The lower mantle is based on the TX2011 tomography model (Grand, 2002). B: Same as panel A, but computed from the GLAD-M25 (Lei et al., 2020) tomography model in the upper mantle and S362ANI+M tomography model (Moulik & Ekström, 2014) in the transition zone and lower mantle. C & D: Same model as in A & B, respectively, plotted in cross section from west to east (see map inset for location) and from the surface to the CMB.

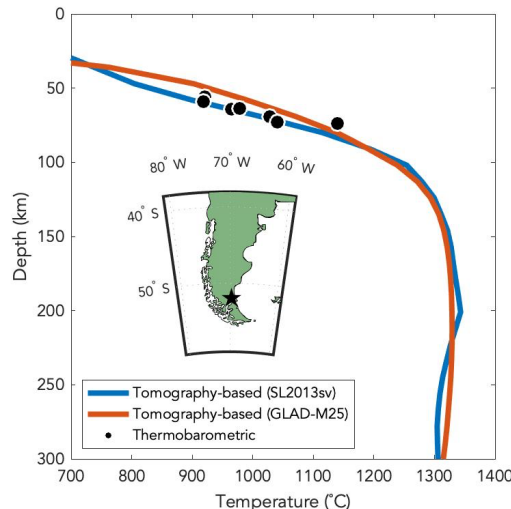


Figure 5.

522
523
524
525
526
527
528
529
530
531

Thermobarometric estimates of mantle xenoliths (black points) that erupted in the Pali-Aike Volcanic Field (star in inset) over the Plio-Quaternary. These estimates of shallow mantle temperatures and pressures agree with local temperature models independently calculated from tomographic models. The blue and red profiles show the depth variations in temperature from a SL2013sv and GLAD-M25-derived upper mantle models, respectively.

3.2.2 Mantle flow

The temperature and corresponding 3-D viscosity models are used to produce predictions of mantle flow. Our models show that warm temperatures and low viscosities beneath the Antarctic plate promote inflow of hot asthenosphere through the slab window (Fig. 4)—an established slab window mantle flow pattern that has been studied in both laboratory and field settings (e.g., Guillaume et al., 2010; Thorkelson et al., 2011). In the transition zone, colder and stiffer material is downwelling, which when combined with overlying westerly inflow, produces a north-south axial convection cell in the upper half of the mantle (Fig. 4C,D). This flow scheme is ubiquitous across the suite of convection simulations, despite notable differences in initial temperature structures. The cross section at ~100 km depth shows flow velocities from models that include SL2013sv-derived upper mantle structure also reflect inflow from beneath the Antarctic plate and exhibit a weakly to moderately developed toroidal component, as edge driven convection delivers material northward along the southern boundary of the subducting Nazca slab (Fig. 4A). Recent results from surface wave azimuthal anisotropy, which are sensitive to depths of ~100 km, agree with our prediction of westerly inflow through the slab window and toroidal circulation northward, which is seen in some of our simulations (Fig. 4A; Wiens et al., 2021).

In the mantle transition zone, our convection models predict downwelling of the relatively cold and high viscosity structure associated with the relict Nazca slab; however, flow slows across the 660 km discontinuity due to a general increase in viscosity. Global geochemical, geodynamic, and geophysical evidence indicates that the transition zone acts as a heterogeneous boundary, where upwellings more easily penetrate than downwellings, with

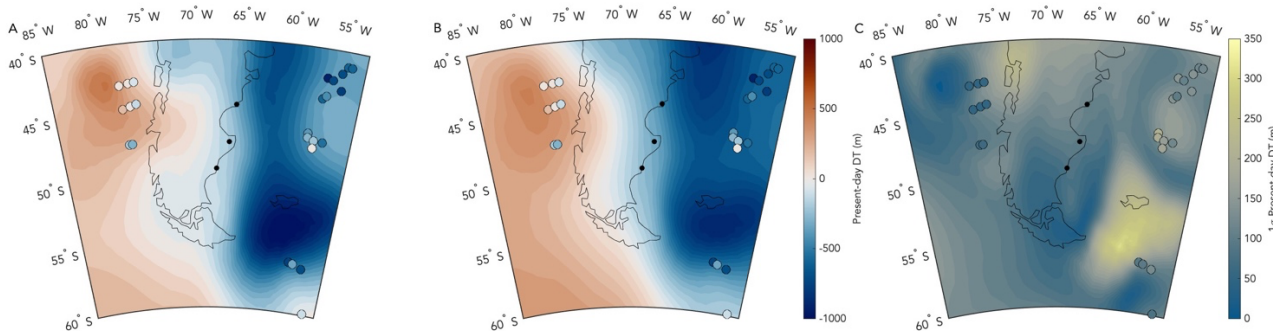
553 periodic ‘avalanches’ of cold material facilitating exchange (Behn et al., 2004; Gautheron &
 554 Moreira, 2002; Meyzen et al., 2007; Tackley et al., 1994). The endothermic phase transition
 555 from ringwoodite (or similar compositions) to bridgemanite plays a key role in hampering slab
 556 descent (e.g., Bina et al., 2001; Chanyshchev et al., 2022; Faccenda & Dal Zilio, 2017; Goes et al.,
 557 2017). Our mantle temperature and viscosity models reflect these dynamics as the presence of
 558 the geometrically diffuse formerly subducted Nazca slab may suggest temporary slab stagnation
 559 or ponding in the transition zone. In general, slab dynamics in the transition zone have the
 560 capacity to modulate the extent of uplift at the surface. As such, beneath Patagonia the
 561 predicted slab stagnation appears to hamper overall downwelling that might otherwise
 562 counteract uplift driven by overlying low viscosity throughflow from beneath the Antarctic plate
 563 (Fig. 4C,D).

564

565 3.2.3 Present-day dynamic topography

566 The best-fitting (described in detail in section 3.3) DT change solution corresponds to a
 567 present-day prediction derived from SL2013sv upper mantle and TX2011 transition zone and
 568 lower mantle structure paired with the V2 viscosity profile. The resulting flow field produces a
 569 positive topographic anomaly in the South Pacific that extends across the Patagonian continent
 570 at the latitude of the slab window, 45°S – 50°S, before transitioning to a negative DT signal in the
 571 South Atlantic Ocean (Fig. 6A). This asymmetric pattern occurs systematically across the
 572 convection suite. The positive DT signature over the South Pacific reflects hot, buoyant mantle
 573 upwelling associated with the Nazca-Antarctic Ridge. Off the eastern coast, our negative DT
 574 predictions coincide with the Argentine Abyssal Plain, a 2000 km-wide region of anomalously
 575 deep bathymetry that has been hypothesized to be one of the largest convective drawdowns on
 576 Earth (Hoggard et al., 2016; Hohertz & Carlson, 1998). While our preferred model predicts
 577 positive present-day DT directly overlying the slab gap, the eastern coast sits between these two
 578 regions of positive and negative DT and as such represents an active geodynamic setting (Fig.
 579 6A). The longitudinal pattern reflects a more symmetric arc that peaks near 46°S, which is in
 580 agreement with the present-day DT results from Flament et al. (2015). The mean present-day
 581 DT prediction yields a similar asymmetrical spatial pattern from west to east, but unlike the
 582 preferred solution, it predicts a more diffuse positive anomaly that transitions to negative
 583 present-day DT at about 70°W (Fig. 6A,B).

584



585

586

587

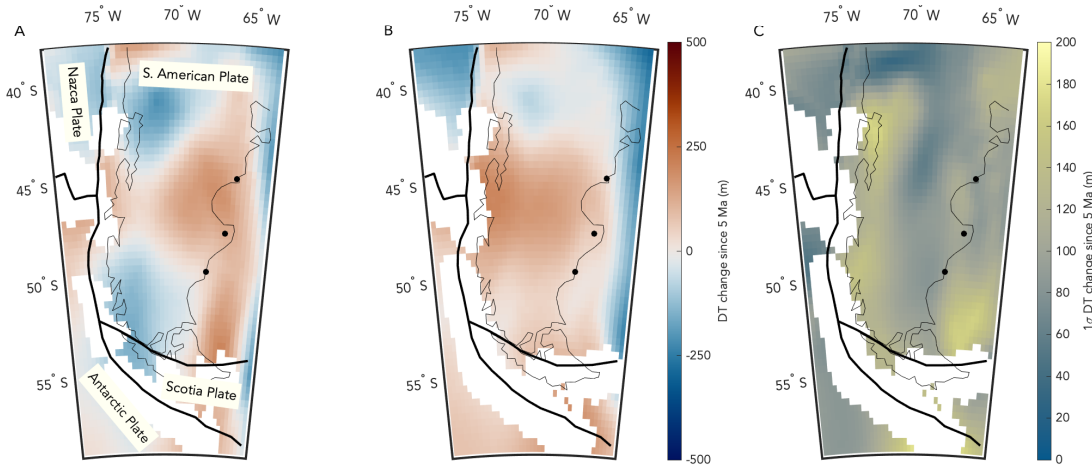
Figure 6.

588 Present-day DT and residual topography measurements. A: Best fitting present-day DT with SL2013sv upper mantle
589 and TX2011 transition zone and lower mantle-derived structure (Grand et al., 2002; Schaeffer & Lebedev, 2013).
590 This model uses the V2 viscosity profile. Colored circles show residual topography measurements from Hoggard et
591 al. (2017). B: Mean present-day DT prediction from entire convection suite. C: 1σ uncertainty of present-day DT
592 and residual topography measurements (circles).

593
594 Since our simulations treat the oceanic lithosphere as neutrally buoyant, we can compare
595 our predictions to the local residual topography estimates from Hoggard et al. (2017), which
596 were obtained by removing the ocean cooling trend from the observed topography (in addition
597 to crustal, sedimentary loading, and geoid corrections). Despite some sign disagreement over
598 the Nazca and Antarctic plates to the west where the residual topography estimates may begin
599 to be contaminated by flexure of the down-going plate beneath the Andean subduction zone,
600 the models and the local residual topography data agree to first order, in particular over the
601 Argentine Abyssal Plain, where negative residual topography has been mapped (Fig. 6A,B) and
602 the mantle is downwelling due to the presence of the cold, remnant Nazca slab residing in the
603 mantle transition zone (Fig. 4C,D). Divergence in data-model comparison likely stems from
604 tomographic inaccuracies and locally-important anomalies in lithospheric thickness, which we do
605 not capture in our convection models. While our model suite systematically captures this
606 asymmetrical DT pattern across the region, the models that includes upper mantle structure
607 from SL2013sv, instead of GLAD-M25, achieve better fits to the residual topography
608 measurements (see section 3.3).
609

610 3.2.4 Dynamic topography change

611 The change in DT that results from our suite of time-evolving mantle flow models varies
612 from >300 m of uplift to >100 m of subsidence across the eastern coast of Patagonia. The mean
613 DT change prediction of the full suite, however, is characterized by a broad region of positive
614 uplift across the foreland (Fig. 7B). Some models also predict uplift to the southeast of the slab
615 window (e.g., Fig. 7A), but this anomaly remains untested due to the absence of regional DT
616 change observations. While the mean of our DT change predictions indicates uplift across the
617 eastern coast (Fig. 7B), the associated uncertainties at the three paleo shorelines are
618 prohibitively large (22.3 ± 104.1 m, 105.2 ± 102.7 m, and -5.1 ± 98.4 m, 1σ from south to north)
619 to employ as a correction and as such preclude a meaningful inference of GMSL (Fig. 7C). In
620 section 3.3, we leverage additional data to isolate best-fitting models that ultimately can be used
621 as DT change corrections, enabling an inference of GMSL. We found that this step was crucial
622 for robustly correcting shoreline elevations for DT change.
623

624
625

626

627

628 Change in DT predictions across Patagonian foreland. A: Best-fitting (lowest MSWD) change in DT since the early
 629 Pliocene. This solution uses a mantle temperature model calculated from TX2011 (Grand, 2002) seismic velocities in
 630 the transition zone and lower mantle and SL2013 (Schaeffer & Lebedev, 2013) in the upper mantle. White-out area
 631 reflects regions where the crust that has either been formed or subducted since 5 Ma, due to the rotation of
 632 tectonic plates over the 5-Myr model timespan. B: The mean DT change for the full convection suite. C: 1σ
 633 uncertainty from the mean prediction in B.

634

635 From south to north, our models predict variable DT change (Fig. 8). Profiles along the
 636 eastern coast through the three shorelines show that the majority of models produces a broad,
 637 arc-shaped pattern of DT change with the peak centered on the middle site (Fig. 8). Note that
 638 our sampling procedure contributes to this similarity in shape, as we select from sites that best
 639 fit the differential elevations of the shorelines (see section 2.3). As such, 50 out of 90 of our DT
 640 change models predict an MSWD fit to the three shorelines of lower than 5. Many of these low-
 641 MSWD models predict significant subsidence (Fig. 8), however, which is physically unlikely as it
 642 would imply sea level in the early Pliocene was lower than today. In spite of this wide range,
 643 several models, which represent the uplift histories most consistent with geodynamic
 644 observables (see section 3.3), fall in an intermediate range while also achieving good fits to the
 645 GIA-corrected shoreline elevations (Fig. 8).

646

Figure 7.

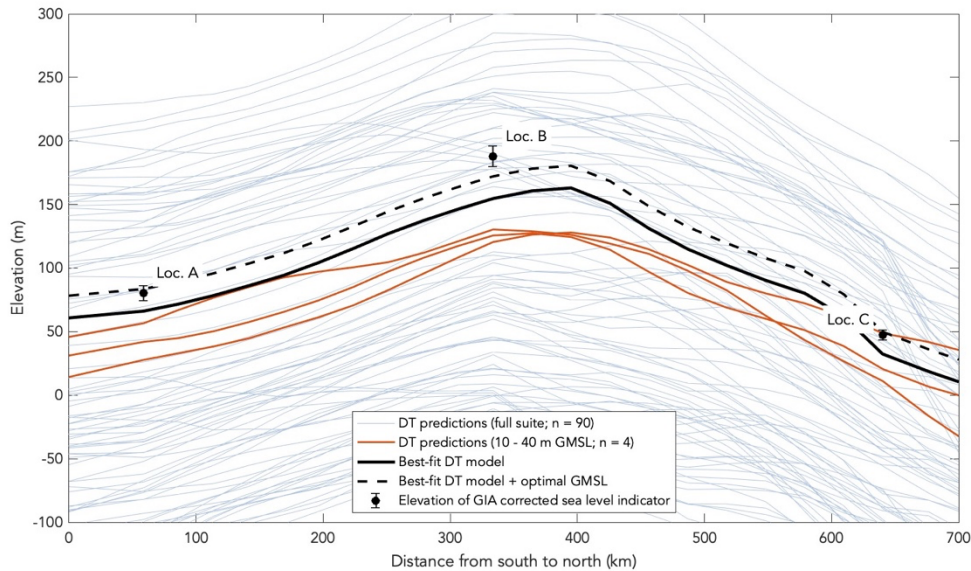


Figure 8.

647
648
649
650
651
652
653
654
655
656
657
658
659
660
661
662
663
664
665
666
667
668
669
670
671
672
673
674
675
676

Great circle profiles of DT change across the Patagonian foreland from south to north through the three sea level indicator sites. GIA-corrected elevations are shown by black markers (uncertainties are 1σ). Red profiles show DT change predictions that lead to GMSL estimates within 10 – 40 m. While these predictions correspond to more realistic GMSLs, many achieve poor fits to the GIA-corrected shoreline elevations. The best fitting model is shown in black and its associated sea level prediction including GMSL inference is shown as the black dashed line.

Past studies have suggested that the Patagonian slab window is a likely setting for ongoing dynamic uplift, which we confirm here (Dávila et al., 2019; Dávila & Lithgow-Bertelloni, 2013; Flament et al., 2015; Guillaume et al., 2009, 2010, 2013). Flament et al. (2015) modeled time-dependent flow, and their most recent DT change predictions (~10 Ma to present) generally agree with our suite of DT change scenarios, indicating broad regional uplift across the Patagonian foreland. Trench-parallel tilted fluvial terraces located north and south of $\sim 46.5^\circ\text{S}$ are among limited geomorphological evidence of DT change in Patagonia that have been used to ground truth models. Separately, Guillaume et al. (2009) and Flament et al. (2015) used these features to validate geodynamic models of northward migration of the CTJ during the Miocene. As these terraces and their tilting predate the time range of our convection models, we cannot comment on their initial tilting history; however, our DT change predictions, which span a time interval over which the CTJ has remained stable (Breitsprecher & Thorkelson, 2009), would drive no additional structural contamination of these features as is consistent with current field mapping (Guillaume et al., 2009). Our DT change predictions may, however, explain northward tilting of Pleistocene marine terraces mapped by Pedoja et al. (2011) located along the eastern coast of Argentina north of our study area, as our models show a positive anomaly extending from the northernmost early-Pliocene shoreline transitioning to increasingly negative DT change farther north (Fig. 7A,B). That said, our models do not target DT change over the Pleistocene and should be compared to these observations cautiously.

677 3.3 Implications for Earth model and GMSL when combining multiple constraints

678 3.3.1 Best fitting Earth model

679 In section 3.2 we describe how our model predictions compare to various observations in
680 isolation. Here, we now seek to investigate which Earth structure performs best in matching all
681 observations simultaneously. In addition to the MSWD, which provides a metric for how well a
682 specific Earth model fits the variation in GIA-corrected elevations of the three paleo shorelines,
683 we use the following three screening criteria: (1) the GMSL prediction is limited to a range of 10
684 to 40 m; (2) the fit to local residual topography measurements (MSWD) has to be less than 20;
685 and (3) GIA and DT-corrected GMSL in Mallorca (using same models applied in Patagonia) should
686 vary by less than 5 m from the value inferred from Argentina. Only 4 of the 90 total predictions
687 satisfy the constraint of yielding GMSL between 10 to 40 m (Fig. 6). Restricting the total suite to
688 those predictions that have an MSWD fits to local residual topography measurements of less
689 than 20 results in 65 models. Twenty-four models satisfy the requirement of GMSL consistency
690 within 5 m between Argentina and Mallorca. Only 1 of the 90 models satisfy all of these
691 constraints jointly. This model consists of TX2011-derived transition zone and lower mantle
692 structure and SL2013sv-derived upper mantle structure paired with the V2 viscosity profile,
693 representing the single best convection parameterization within the suite. This best-fitting
694 ($\text{MSWD} = 1.54$) DT change field used a total rotation of 1.8° ($0.36^\circ \text{ Myr}^{-1} \times 5 \text{ Myrs}$). Notably,
695 Steinberger (2016) used several different tomography-derived mantle structures to predict
696 present-day geodynamic observables and also found that a combination of SL2013sv and TX2011
697 had the greatest success.

698 In addition to identifying preferred Earth structure from the best-fitting prediction, we
699 consider the success of convection parameters of the entire suite by computing the mean
700 (averaged over the plate rotations) MSWD of each viscosity-temperature model pair for fits to
701 both the three shorelines in Argentina and local residual topography measurements. This
702 reveals that the V1 viscosity profile paired with GLAD-M25 upper mantle and S4ORTS transition
703 zone and lower mantle structure achieves the best mean fit to the differential elevations of the
704 three shorelines in Argentina (Fig. 9A). That said, this temperature model fails to achieve a good
705 fit (mean $\text{MSWD} > 20$) to local residual topography measurements for all three viscosity profiles
706 (Fig. 9B). The only temperature model that achieves low mean $\text{MSWD} (< \sim 10)$ fits for the three
707 paleo shorelines in Argentina across all three viscosity profiles is the SL2013sv upper mantle and
708 S4ORTS transition zone and lower mantle-derived model (Fig. 9A). Models with SL2013sv-
709 derived upper mantle structure systematically correspond to better MSWD fits with local
710 residual topography measurements in comparison with those that include GLAD-M25-derived
711 upper mantle structure (Fig. 9B). In addition to their success in fitting observations of present-
712 day DT and DT change, SL2013sv-based convection simulations also prove better at reproducing
713 toroidal flow that has been constrained by surface wave azimuthal anisotropy (Wiens et al.,
714 2021). This likely reflects the higher resolution of SL2013sv compared to GLAD-M25, which may
715 be attributed to its use of shorter period surface wave data. Lastly, a systematic preference for
716 the mantle viscosity structure remains elusive, likely due to the close similarity amongst the
717 three profiles tested (Fig. 2A).

718

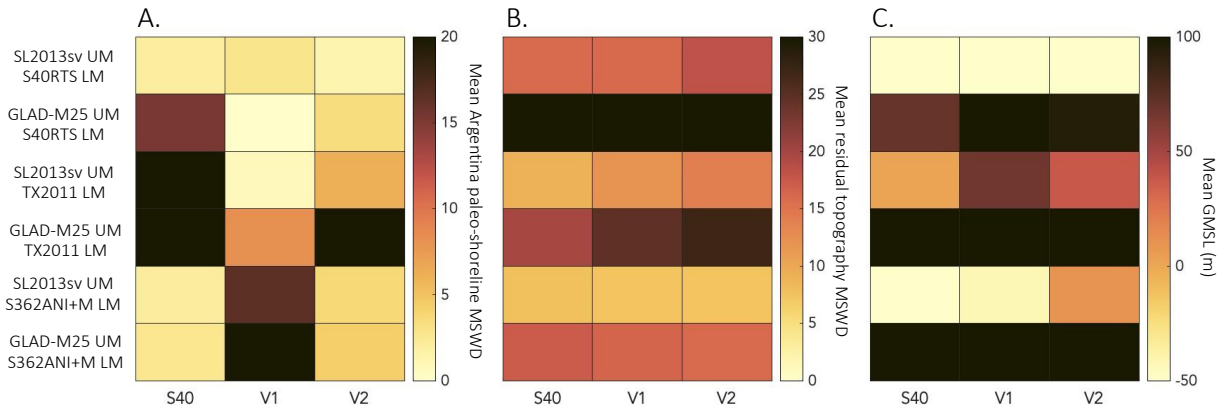


Figure 9.

Analysis of temperature and viscosity model parameterization. A: Heatmap of the mean MSWD that describes how well each convection simulation matches the differential elevations of the paleo-shorelines. B: Heatmap of the mean MSWD describing the fit between the predicted and observed residual topography. Note that a low MSWD indicates a better fit. C: Mean GMSL prediction for each simulation (based on results for the 5 different total lithospheric rotation values).

3.3.2 GMSL inference

After correcting the observed elevations for GIA and DT change since the early Pliocene, the remaining offset between the model and the corrected elevations reflects GMSL during the time of deposition. The best-fitting DT change solution (lowest MSWD for the shoreline) yields a GMSL of 17.5 ± 6.4 m. This uncertainty is driven by uncertainties in the GIA correction, the measurement uncertainty, and variability across the three sites (Eq. 8). This GMSL value falls within the lower bounds of the uncertainty of the GMSL estimate from Mallorca, Spain where a GMSL of 25.1 m (10.6 to 28.3 m 16th and 84th uncertainty bounds) was inferred from a sea-level indicator dated to 4.39 ± 0.39 Ma (Dumitru et al., 2019). Using just the northernmost Patagonian shoreline, Rovere et al. (2020) reported a GMSL of 28.4 ± 11.7 m. An estimate of GMSL of 23.4 ± 35.8 m (mean, 1σ) from sea level indicators from South Africa was corrected for GIA and DT change (Hearty et al., 2020; Rovere et al., 2020). The large uncertainties in both of these estimates stem from DT corrections that were not constrained by local observations. In South Africa in particular, this correction is expected to be challenging due to the Large Low-Shear-Velocity Province (LLSVP) which directly underlies this part of the globe at the CMB. This geodynamic structure has uncertain internal compositional heterogeneity and vertical extent, making it difficult to accurately parameterize within convection simulations (Richards et al., 2021).

We test the sensitivity of our final GMSL estimate to the screening criteria above by adjusting the aforementioned thresholds. We find that a threshold of 10 m agreement between the GMSL estimate in Mallorca and Argentina isolates just 2 additional models. Relaxing the MSWD threshold for local residual topography from 20 to 30 satisfies 10 additional simulations. However, none of these additional models satisfy our criteria that GMSL must fall within 10 – 40 m.

753 In an early Pliocene climate context, when global mean temperatures were $\sim 4^{\circ}\text{C}$ higher
754 than they are today, a GMSL of 17.5 ± 6.4 m (1σ) would require the absence of large sectors of
755 Earth's modern ice sheets. The Greenland Ice Sheet (GIS) was likely small during this time period
756 accounting for around 6 – 7 m in GMSL difference between the early Pliocene and today
757 (Bierman et al., 2016). Thermal expansion may explain an additional 1.5 m (Dumitru et al.,
758 2019). This leaves approximately 9.5 ± 6.9 m, which must be sourced from Antarctica, likely
759 coming from the WAIS and parts of marine-based sectors of the EAIS.

760

761 4. Conclusion

762

763 We employ the latest results from seismic tomography, rheological mapping, and
764 numerical mantle convection modeling to predict DT changes along the eastern Patagonia
765 margin. We find that DT change can explain the different elevations of three sea-level indicators
766 supporting the hypothesis that mantle convection plays a major role in deforming Pliocene paleo
767 shorelines (Rovere et al., 2014; Rowley et al., 2013). Our models indicate dynamic upwarping
768 driven primarily by a well-developed north-south axial circulation cell across the slab window
769 that delivers hot asthenosphere from beneath the Antarctic plate through a slab window. The
770 lower branch of the cell is driven by subducting Nazca slab, which might be ponding near the 670
771 km discontinuity. Shallow (~ 100 km) tangential flow is characterized by a toroidal component
772 located in the vicinity of $45^{\circ}\text{S}, 72^{\circ}\text{W}$ that is in agreement with constraints from surface wave
773 anisotropy (Wiens et al., 2021).

774 We constrain the flow pattern to match the deformation observed along the Patagonian
775 margin at the three shorelines and apply additional criteria to identify the most likely flow field
776 and amount of deformation. Without applying these constraints, DT predictions vary by >400 m,
777 which highlights the sensitivity of DT predictions to small changes in the parameters used in the
778 convection modeling. This implies that studies that use a limited set of convection models that
779 are not constrained by additional local observations can lead to erroneous results.

780 We find that models with an upper mantle structure derived from SL2013sv (Schaeffer &
781 Lebedev, 2013) combined with a transition zone and lower mantle structure from TX2011 (Grand
782 et al., 2002) yield the best fit to observations, in line with previous work that focused on present-
783 day DT (Richards et al., 2020; Steinberger, 2016b). Correcting shorelines for GIA and DT yields a
784 best GMSL estimate of 17.5 ± 6.4 m above present-day for the early Pliocene, an interval when
785 temperatures and CO_2 were significantly higher than today (Fedorov et al., 2013; Pagani et al.,
786 2010; Seki et al., 2010). This estimate overlaps with that from Mallorcan speleothem records
787 and provides mounting evidence that early Pliocene sea level was significantly higher than today,
788 making it an important calibration target for ice sheet models.

789

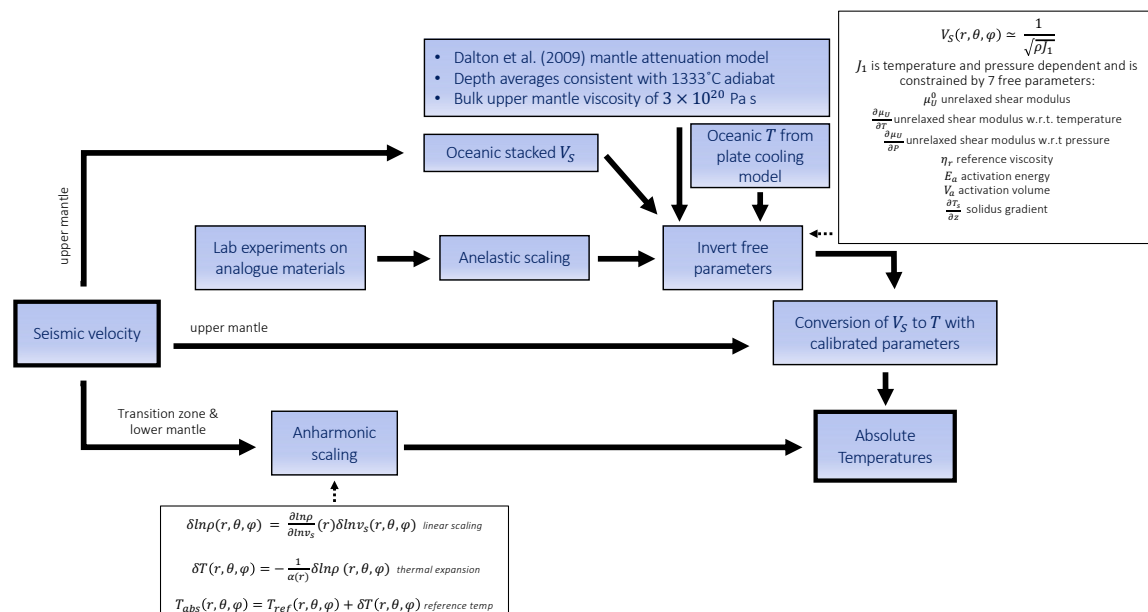
790 Acknowledgements

791

792 We acknowledge computing resources from Columbia University's Shared Research
793 Computing Facility project, which is supported by NIH Research Facility Improvement Grant
794 1G20RR03893-01, and associated funds from the New York State Empire State Development,
795 Division of Science Technology and Innovation (NYSTAR) Contract C090171, both awarded April
796 15th, 2010. We thank the Computational Infrastructure for Geodynamics (geodynamics.org)

which is funded by the National Science Foundation under award EAR-0949446 and EAR-1550901 for supporting the development of ASPECT. The authors acknowledge PALSEA, a working group of the International Union for Quaternary Sciences (INQUA) and Past Global Changes (PAGES), which in turn received support from the Swiss Academy of Sciences and the Chinese Academy of Sciences. JA acknowledges funding from the Alfred P. Sloan Research Fellowship FG-2021-15970. FDR thanks the Imperial College Research Fellowship and Schmidt Science Fellow schemes. MH acknowledges support from the Australian Research Council DECRA DE220101519 and the Australian Government's *Exploring for the Future* program.

Supplementary Materials



808
809
810
811

Supplementary Figure 1.

812 Workflow of seismic velocity to temperature conversion. In the lower mantle, we apply a simple anharmonic scaling
813 that converts velocity to density and uses a depth-varying thermal expansivity (Glišović & Forte, 2015) and a
814 reference temperature of 1333°C. In the upper mantle, we use a laboratory-based constraint on anelastic
815 deformation of the mantle analogue material, borneol, calibrated with independent geophysical observations of the
816 upper mantle (Yamauchi & Takei, 2016; Richards et al., 2020; see section 2.2). This conversion exploits oceanic
817 lithospheric temperatures from a plate cooling model (Richards et al., 2018) in an inverse scheme that identifies
818 seven free parameters (box to the right) from the Yamauchi & Takei (2016) anelastic conversion. In addition, this
819 inverse parameterization enforces a bulk upper mantle viscosity of 3×10^{20} Pa s, depth-averaged temperatures
820 consistent with a 1333°C adiabat, and an attenuation structure in agreement with that of Dalton et al. (2009). The
821 final parameterization (7 values) is specific to each tomography model.

822
823
824
825

826

Supplementary table 1
Upper mantle seismic velocity to temperature conversion parameters.

	SL2013sv	GLAD-M25
mu0 (Gpa)	76.33	80.82
dmudT (Gpa °C ⁻¹)	-0.01771	-0.02
dmudP	2.529	2.292
eta0 (Pa s)	1.23×10^{21}	2.00×10^{23}
Ea (kJ mol ⁻¹)	2.02×10^5	545
Va (cm ³ mol ⁻¹)	1.92×10^{-6}	0.9633
solgrad (°C km ⁻¹)	0.955	0.8634

827

828

Supplementary table 2
Thermobarometry calculation for Pali-Aike mantle xenoliths.

Longitude (°)	Latitude (°)	Pressure (kbar)	Temperature (°C)
-69.7883	-52.075	24.11	1140.27
-70.2044	-52.0161	18.24	920.27
-70.2044	-52.0161	20.91	964.31
-69.7883	-52.075	22.49	1028.31
-70.2044	-52.0161	19.27	918.48
-70.0689	-52.0397	20.81	978.27
-69.68	-51.82	23.77	1040.77

829

830

831

832

833

834

835

836

837

838

839

840

841

842

843

844 References

- 845
846 An, M., Wiens, D. A., Zhao, Y., Feng, M., Nyblade, A., Kanao, M., Li, Y., Maggi, A., & Lévêque, J.-J.
847 (2015). Temperature, lithosphere–asthenosphere boundary, and heat flux beneath the
848 Antarctic Plate inferred from seismic velocities. *Journal of Geophysical Research: Solid*
849 *Earth*, 120(12), 8720–8742. <https://doi.org/10.1002/2015JB011917>
- 850 Argus, D. F., Gordon, R. G., & DeMets, C. (2011). Geologically current motion of 56 plates relative
851 to the no-net-rotation reference frame. *Geochemistry, Geophysics, Geosystems*, 12(11).
852 <https://doi.org/10.1029/2011GC003751>
- 853 Austermann, J., & Mitrovica, J. X. (2015). Calculating gravitationally self-consistent sea level
854 changes driven by dynamic topography. *Geophysical Journal International*, 203(3), 1909–
855 1922. <https://doi.org/10.1093/gji/ggv371>
- 856 Austermann, J., Mitrovica, J. X., Huybers, P., & Rovere, A. (2017). Detection of a dynamic
857 topography signal in last interglacial sea-level records. *Science Advances*, 3(7), e1700457.
858 <https://doi.org/10.1126/sciadv.1700457>
- 859 Bangerth, W., Dannberg, J., Gassmoeller, R., Heister, T., & others. (2020). *ASPECT: Advanced*
860 *Solver for Problems in Earth's Convection, User Manual*.
861 <https://doi.org/10.6084/m9.figshare.4865333.v7>
- 862 Behn, M. D., Conrad, C. P., & Silver, P. G. (2004). Detection of upper mantle flow associated with
863 the African Superplume. *Earth and Planetary Science Letters*, 224(3), 259–274.
864 <https://doi.org/10.1016/j.epsl.2004.05.026>
- 865 Bhanot, K. K., Downes, H., Petrone, C. M., Humphreys-Williams, E., & Clark, B. (2020). Micro-CT
866 investigation of garnet-spinel clusters in mantle peridotite xenoliths. *Lithos*, 352–353,
867 105250. <https://doi.org/10.1016/j.lithos.2019.105250>
- 868 Bierman, P. R., Shakun, J. D., Corbett, L. B., Zimmerman, S. R., & Rood, D. H. (2016). A persistent
869 and dynamic East Greenland Ice Sheet over the past 7.5 million years. *Nature*, 540(7632),
870 256–260. <https://doi.org/10.1038/nature20147>
- 871 Bina, C. R., Stein, S., Marton, F. C., & Van Ark, E. M. (2001). Implications of slab mineralogy for
872 subduction dynamics. *Physics of the Earth and Planetary Interiors*, 127(1), 51–66.
873 [https://doi.org/10.1016/S0031-9201\(01\)00221-7](https://doi.org/10.1016/S0031-9201(01)00221-7)
- 874 Breitsprecher, K., & Thorkelson, D. J. (2009). Neogene kinematic history of Nazca–Antarctic–
875 Phoenix slab windows beneath Patagonia and the Antarctic Peninsula. *Tectonophysics*,
876 464(1), 10–20. <https://doi.org/10.1016/j.tecto.2008.02.013>
- 877 Burke, K. D., Williams, J. W., Chandler, M. A., Haywood, A. M., Lunt, D. J., & Otto-Bliesner, B. L.
878 (2018). Pliocene and Eocene provide best analogs for near-future climates. *Proceedings*
879 *of the National Academy of Sciences*, 115(52), 13288–13293.
880 <https://doi.org/10.1073/pnas.1809600115>
- 881 Chanyshhev, A., Ishii, T., Bondar, D., Bhat, S., Kim, E. J., Farla, R., Nishida, K., Liu, Z., Wang, L.,
882 Nakajima, A., Yan, B., Tang, H., Chen, Z., Higo, Y., Tange, Y., & Katsura, T. (2022).
883 Depressed 660-km discontinuity caused by akimotoite–bridgmanite transition. *Nature*,
884 601(7891), 69–73. <https://doi.org/10.1038/s41586-021-04157-z>
- 885 Collins, M., Knutti, R., Arblaster, J., Dufresne, J.-L., Fichefet, T., Friedlingstein, P., Gao, X.,
886 Gutowski, W. J., Johns, T., Krinner, G., Shongwe, M., Tebaldi, C., Weaver, A. J., Wehner,
887 M. F., Allen, M. R., Andrews, T., Beyerle, U., Bitz, C. M., Bony, S., & Booth, B. B. B. (2013).

- 888 Long-term Climate Change: Projections, Commitments and Irreversibility. *Climate Change*
889 *2013 - The Physical Science Basis: Contribution of Working Group I to the Fifth Assessment*
890 *Report of the Intergovernmental Panel on Climate Change*, 1029–1136.
- 891 Cook, C. P., van de Flierdt, T., Williams, T., Hemming, S. R., Iwai, M., Kobayashi, M., Jimenez-
892 Espejo, F. J., Escutia, C., González, J. J., Khim, B.-K., McKay, R. M., Passchier, S., Bohaty, S.
893 M., Riesselman, C. R., Tauxe, L., Sugisaki, S., Galindo, A. L., Patterson, M. O., Sangiorgi, F.,
894 ... Yamane, M. (2013). Dynamic behaviour of the East Antarctic ice sheet during Pliocene
895 warmth. *Nature Geoscience*, 6(9), 765–769. <https://doi.org/10.1038/ngeo1889>
- 896 Dalton, C. A., Ekström, G., & Dziewonski, A. M. (2009). Global seismological shear velocity and
897 attenuation: A comparison with experimental observations. *Earth and Planetary Science
898 Letters*, 284(1–2), 65–75. <https://doi.org/10.1016/j.epsl.2009.04.009>
- 899 Dávila, F., Avila, P., Martina, F., Canelo, H., Nóbile, J., Collo, G., Nassif, F., & Ezpeleta, M. (2019).
900 *Measuring dynamic topography in South America* (pp. 35–66).
901 <https://doi.org/10.1016/B978-0-12-816009-1.00003-4>
- 902 Dávila, F. M., & Lithgow-Bertelloni, C. (2013). Dynamic topography in South America. *Journal of
903 South American Earth Sciences*, 43, 127–144.
904 <https://doi.org/10.1016/j.jsames.2012.12.002>
- 905 DeConto, R. M., & Pollard, D. (2016). Contribution of Antarctica to past and future sea-level rise.
906 *Nature*, 531(7596), 591–597. <https://doi.org/10.1038/nature17145>
- 907 DeConto, R. M., Pollard, D., Alley, R. B., Velicogna, I., Gasson, E., Gomez, N., Sadai, S., Condron,
908 A., Gilford, D. M., Ashe, E. L., Kopp, R. E., Li, D., & Dutton, A. (2021). The Paris Climate
909 Agreement and future sea-level rise from Antarctica. *Nature*, 593(7857), 83–89.
910 <https://doi.org/10.1038/s41586-021-03427-0>
- 911 del Río, C. J., Griffin, M., McArthur, J. M., Martínez, S., & Thirlwall, M. F. (2013). Evidence for
912 early Pliocene and late Miocene transgressions in southern Patagonia (Argentina):
913 $^{87}\text{Sr}/^{86}\text{Sr}$ ages of the pectinid “Chlamys” actinodes (Sowerby). *Journal of South American
914 Earth Sciences*, 47, 220–229. <https://doi.org/10.1016/j.jsames.2013.08.004>
- 915 Dumitru, O. A., Austermann, J., Polyak, V. J., Fornós, J. J., Asmerom, Y., Ginés, J., Ginés, A., &
916 Onac, B. P. (2019). Constraints on global mean sea level during Pliocene warmth. *Nature*,
917 574(7777), 233–236. <https://doi.org/10.1038/s41586-019-1543-2>
- 918 Dutton, A., Carlson, A. E., Long, A. J., Milne, G. A., Clark, P. U., DeConto, R., Horton, B. P.,
919 Rahmstorf, S., & Raymo, M. E. (2015). Sea-level rise due to polar ice-sheet mass loss
920 during past warm periods. *Science*, 349(6244). <https://doi.org/10.1126/science.aaa4019>
- 921 Dziewonski, A. M., & Anderson, D. L. (1981). Preliminary reference Earth model. *Physics of the
922 Earth and Planetary Interiors*, 25(4), 297–356. [https://doi.org/10.1016/0031-9201\(81\)90046-7](https://doi.org/10.1016/0031-
923 9201(81)90046-7)
- 924 Eagles, G. (2004). Tectonic evolution of the Antarctic–Phoenix plate system since 15 Ma. *Earth
925 and Planetary Science Letters*, 217(1), 97–109. [https://doi.org/10.1016/S0012-821X\(03\)00584-3](https://doi.org/10.1016/S0012-
926 821X(03)00584-3)
- 927 Faccenda, M., & Dal Zilio, L. (2017). The role of solid–solid phase transitions in mantle
928 convection. *Lithos*, 268–271, 198–224. <https://doi.org/10.1016/j.lithos.2016.11.007>
- 929 Fedorov, A. V., Brierley, C. M., Lawrence, K. T., Liu, Z., Dekens, P. S., & Ravelo, A. C. (2013).
930 Patterns and mechanisms of early Pliocene warmth. *Nature*, 496(7443), 43–49.
931 <https://doi.org/10.1038/nature12003>

- 932 Fischer, H., Meissner, K. J., Mix, A. C., Abram, N. J., Austermann, J., Brovkin, V., Capron, E.,
933 Colombaroli, D., Daniau, A.-L., Dyez, K. A., Felis, T., Finkelstein, S. A., Jaccard, S. L.,
934 McClymont, E. L., Rovere, A., Sutter, J., Wolff, E. W., Affolter, S., Bakker, P., ... Zhou, L.
935 (2018). Palaeoclimate constraints on the impact of 2 °C anthropogenic warming and
936 beyond. *Nature Geoscience*, 11(7), 474–485. <https://doi.org/10.1038/s41561-018-0146-0>
- 937 Flament, N., Gurnis, M., Müller, R. D., Bower, D. J., & Husson, L. (2015). Influence of subduction
938 history on South American topography. *Earth and Planetary Science Letters*, 430, 9–18.
939 <https://doi.org/10.1016/j.epsl.2015.08.006>
- 940 Forte, A. M., Peltier, W. R., Dziewonski, A. M., & Woodward, R. L. (1993). Dynamic surface
941 topography: A new interpretation based upon mantle flow models derived from seismic
942 tomography. *Geophysical Research Letters*, 20(3), 225–228.
943 <https://doi.org/10.1029/93GL00249>
- 944 Forte, A. M., Quéré, S., Moucha, R., Simmons, N. A., Grand, S. P., Mitrovica, J. X., & Rowley, D. B.
945 (2010). Joint seismic–geodynamic-mineral physical modelling of African geodynamics: A
946 reconciliation of deep-mantle convection with surface geophysical constraints. *Earth and*
947 *Planetary Science Letters*, 295(3), 329–341. <https://doi.org/10.1016/j.epsl.2010.03.017>
- 948 Fulléa, J., Lebedev, S., Martinec, Z., & Celli, N. L. (2021). WINTERC-G: Mapping the upper mantle
949 thermochemical heterogeneity from coupled geophysical–petrological inversion of
950 seismic waveforms, heat flow, surface elevation and gravity satellite data. *Geophysical*
951 *Journal International*, 226(1), 146–191. <https://doi.org/10.1093/gji/ggab094>
- 952 Gautheron, C., & Moreira, M. (2002). Helium signature of the subcontinental lithospheric
953 mantle. *Earth and Planetary Science Letters*, 199(1), 39–47.
954 [https://doi.org/10.1016/S0012-821X\(02\)00563-0](https://doi.org/10.1016/S0012-821X(02)00563-0)
- 955 Glišović, P., & Forte, A. M. (2015). Importance of initial buoyancy field on evolution of mantle
956 thermal structure: Implications of surface boundary conditions. *Geoscience Frontiers*,
957 6(1), 3–22. <https://doi.org/10.1016/j.gsf.2014.05.004>
- 958 Goes, S., Agrusta, R., van Hunen, J., & Garel, F. (2017). Subduction-transition zone interaction: A
959 review. *Geosphere*, 13(3), 644–664. <https://doi.org/10.1130/GES01476.1>
- 960 Goes, S., Govers, R., & Vacher, P. (2000). Shallow mantle temperatures under Europe from P and
961 S wave tomography. *Journal of Geophysical Research: Solid Earth*, 105(B5), 11153–11169.
962 <https://doi.org/10.1029/1999JB900300>
- 963 Gorring, M., Singer, B., Gowers, J., & Kay, S. M. (2003). Plio–Pleistocene basalts from the Meseta
964 del Lago Buenos Aires, Argentina: Evidence for asthenosphere–lithosphere interactions
965 during slab window magmatism. *Chemical Geology*, 193(3), 215–235.
966 [https://doi.org/10.1016/S0009-2541\(02\)00249-8](https://doi.org/10.1016/S0009-2541(02)00249-8)
- 967 Grand, S. P., Davies, J. H., Brodholt, J. P., & Wood, B. J. (2002). Mantle shear-wave tomography
968 and the fate of subducted slabs. *Philosophical Transactions of the Royal Society of*
969 *London. Series A: Mathematical, Physical and Engineering Sciences*, 360(1800), 2475–
970 2491. <https://doi.org/10.1098/rsta.2002.1077>
- 971 Guillaume, B., Gautheron, C., Simon-Labric, T., Martinod, J., Roddaz, M., & Douville, E. (2013).
972 Dynamic topography control on Patagonian relief evolution as inferred from low
973 temperature thermochronology. *Earth and Planetary Science Letters*, 364, 157–167.
974 <https://doi.org/10.1016/j.epsl.2012.12.036>

- 975 Guillaume, B., Martinod, J., Husson, L., Roddaz, M., & Riquelme, R. (2009). Neogene uplift of
976 central eastern Patagonia: Dynamic response to active spreading ridge subduction?
977 *Tectonics*, 28(2). <https://doi.org/10.1029/2008TC002324>
- 978 Guillaume, B., Moroni, M., Funiciello, F., Martinod, J., & Faccenna, C. (2010). Mantle flow and
979 dynamic topography associated with slab window opening: Insights from laboratory
980 models. *Tectonophysics*, 496(1), 83–98. <https://doi.org/10.1016/j.tecto.2010.10.014>
- 981 Guivel, C., Morata, D., Pelleter, E., Espinoza, F., Maury, R. C., Lagabrielle, Y., Polv , M., Bellon, H.,
982 Cotten, J., Benoit, M., Su rez, M., & de la Cruz, R. (2006). Miocene to Late Quaternary
983 Patagonian basalts (46–47°S): Geochronometric and geochemical evidence for slab
984 tearing due to active spreading ridge subduction. *Journal of Volcanology and Geothermal*
985 *Research*, 149(3), 346–370. <https://doi.org/10.1016/j.jvolgeores.2005.09.002>
- 986 Haywood, A. M., Hill, D. J., Dolan, A. M., Otto-Bliesner, B. L., Bragg, F., Chan, W.-L., Chandler, M.
987 A., Contoux, C., Dowsett, H. J., Jost, A., Kamae, Y., Lohmann, G., Lunt, D. J., Abe-Ouchi, A.,
988 Pickering, S. J., Ramstein, G., Rosenbloom, N. A., Salzmann, U., Sohl, L., ... Zhang, Z.
989 (2013). Large-scale features of Pliocene climate: Results from the Pliocene Model
990 Intercomparison Project. *Climate of the Past*, 9(1), 191–209. <https://doi.org/10.5194/cp-9-191-2013>
- 991 Hearty, P. J., Rovere, A., Sandstrom, M. R., O’Leary, M. J., Roberts, D., & Raymo, M. E. (2020).
992 Pliocene-Pleistocene Stratigraphy and Sea-Level Estimates, Republic of South Africa With
993 Implications for a 400 ppmv CO₂ World. *Paleoceanography and Paleoclimatology*, 35(7),
994 e2019PA003835. <https://doi.org/10.1029/2019PA003835>
- 995 Heister, T., Dannberg, J., Gassm ller, R., & Bangerth, W. (2017). High accuracy mantle convection
996 simulation through modern numerical methods – II: Realistic models and problems.
997 *Geophysical Journal International*, 210(2), 833–851. <https://doi.org/10.1093/gji/ggx195>
- 998 Hoggard, M., Austermann, J., Randel, C., & Stephenson, S. (2021). *Observational estimates of*
999 *dynamic topography through space and time*.
1000 <https://eartharxiv.org/repository/view/1997/>
- 1001 Hoggard, M. J., White, N., & Al-Attar, D. (2016). Global dynamic topography observations reveal
1002 limited influence of large-scale mantle flow. *Nature Geoscience*, 9(6), 456–463.
1003 <https://doi.org/10.1038/ngeo2709>
- 1004 Hoggard, M. J., Winterbourne, J., Czarnota, K., & White, N. (2017). Oceanic residual depth
1005 measurements, the plate cooling model, and global dynamic topography. *Journal of*
1006 *Geophysical Research: Solid Earth*, 122(3), 2328–2372.
1007 <https://doi.org/10.1002/2016JB013457>
- 1008 Hohertz, W. L., & Carlson, R. L. (1998). An independent test of thermal subsidence and
1009 asthenosphere flow beneath the Argentine Basin. *Earth and Planetary Science Letters*,
1010 161(1), 73–83. [https://doi.org/10.1016/S0012-821X\(98\)00138-1](https://doi.org/10.1016/S0012-821X(98)00138-1)
- 1011 Jordan, T. H. (1978). Composition and development of the continental tectosphere. *Nature*,
1012 274(5671), 544–548. <https://doi.org/10.1038/274544a0>
- 1013 Kendall, R. A., Mitrovica, J. X., & Milne, G. A. (2005). On post-glacial sea level – II. Numerical
1014 formulation and comparative results on spherically symmetric models. *Geophysical*
1015 *Journal International*, 161(3), 679–706. <https://doi.org/10.1111/j.1365-246X.2005.02553.x>
- 1016
- 1017

- 1018 Kopp, R. E., Simons, F. J., Mitrovica, J. X., Maloof, A. C., & Oppenheimer, M. (2009). Probabilistic
1019 assessment of sea level during the last interglacial stage. *Nature*, 462(7275), 863–867.
1020 <https://doi.org/10.1038/nature08686>
- 1021 Kronbichler, M., Heister, T., & Bangerth, W. (2012). High accuracy mantle convection simulation
1022 through modern numerical methods. *Geophysical Journal International*, 191(1), 12–29.
1023 <https://doi.org/10.1111/j.1365-246X.2012.05609.x>
- 1024 Kulp, S. A., & Strauss, B. H. (2019). New elevation data triple estimates of global vulnerability to
1025 sea-level rise and coastal flooding. *Nature Communications*, 10(1), 4844.
1026 <https://doi.org/10.1038/s41467-019-12808-z>
- 1027 Lei, W., Ruan, Y., Bozdağ, E., Peter, D., Lefebvre, M., Komatitsch, D., Tromp, J., Hill, J., Podhorszki,
1028 N., & Pugmire, D. (2020). Global adjoint tomography—Model GLAD-M25. *Geophysical
1029 Journal International*, 223(1), 1–21. <https://doi.org/10.1093/gji/ggaa253>
- 1030 Lisiecki, L. E., & Raymo, M. E. (2005). A Pliocene-Pleistocene stack of 57 globally distributed
1031 benthic $\delta^{18}\text{O}$ records. *Paleoceanography*, 20(1). <https://doi.org/10.1029/2004PA001071>
- 1032 Livermore, R., Balanyá, J. C., Maldonado, A., Martínez, J. M., Rodríguez-Fernández, J., de
1033 Galdeano, C. S., Zaldívar, J. G., Jabaloy, A., Barnolas, A., Somoza, L., Hernández-Molina, J.,
1034 Suriñach, E., & Viseras, C. (2000). Autopsy on a dead spreading center: The Phoenix
1035 Ridge, Drake Passage, Antarctica. *Geology*, 28(7), 607–610.
1036 [https://doi.org/10.1130/0091-7613\(2000\)28<607:AOADSC>2.0.CO;2](https://doi.org/10.1130/0091-7613(2000)28<607:AOADSC>2.0.CO;2)
- 1037 Lloyd, A. J., Wiens, D. A., Zhu, H., Tromp, J., Nyblade, A. A., Aster, R. C., Hansen, S. E., Dalziel, I. W.,
1038 D., Wilson, T. J., Ivins, E. R., & O'Donnell, J. P. (2020). Seismic Structure of the Antarctic
1039 Upper Mantle Imaged with Adjoint Tomography. *Journal of Geophysical Research: Solid
1040 Earth*, 125(3). <https://doi.org/10.1029/2019JB017823>
- 1041 Meyzen, C. M., Blichert-Toft, J., Ludden, J. N., Humler, E., Mével, C., & Albarède, F. (2007).
1042 Isotopic portrayal of the Earth's upper mantle flow field. *Nature*, 447(7148), 1069–1074.
1043 <https://doi.org/10.1038/nature05920>
- 1044 Mitrovica, J. X., & Forte, A. M. (2004). A new inference of mantle viscosity based upon joint
1045 inversion of convection and glacial isostatic adjustment data. *Earth and Planetary Science
1046 Letters*, 225(1), 177–189. <https://doi.org/10.1016/j.epsl.2004.06.005>
- 1047 Moucha, R., Forte, A. M., Mitrovica, J. X., Rowley, D. B., Quéré, S., Simmons, N. A., & Grand, S. P.,
1048 (2008). Dynamic topography and long-term sea-level variations: There is no such thing as
1049 a stable continental platform. *Earth and Planetary Science Letters*, 271(1), 101–108.
1050 <https://doi.org/10.1016/j.epsl.2008.03.056>
- 1051 Moucha, R., & Ruetenik, G. A. (2017). Interplay between dynamic topography and flexure along
1052 the U.S. Atlantic passive margin: Insights from landscape evolution modeling. *Global and
1053 Planetary Change*, 149, 72–78. <https://doi.org/10.1016/j.gloplacha.2017.01.004>
- 1054 Moulik, P., & Ekström, G. (2014). An anisotropic shear velocity model of the Earth's mantle using
1055 normal modes, body waves, surface waves and long-period waveforms. *Geophysical
1056 Journal International*, 199(3), 1713–1738. <https://doi.org/10.1093/gji/ggu356>
- 1057 Müller, R. D., Hassan, R., Gurnis, M., Flament, N., & Williams, S. E. (2018). Dynamic topography of
1058 passive continental margins and their hinterlands since the Cretaceous. *Gondwana
1059 Research*, 53, 225–251. <https://doi.org/10.1016/j.gr.2017.04.028>
- 1060 Naish, T., Powell, R., Levy, R., Wilson, G., Scherer, R., Talarico, F., Krissek, L., Niessen, F., Pompilio,
1061 M., Wilson, T., Carter, L., DeConto, R., Huybers, P., McKay, R., Pollard, D., Ross, J., Winter,

- 1062 D., Barrett, P., Browne, G., ... Williams, T. (2009). Obliquity-paced Pliocene West Antarctic
1063 ice sheet oscillations. *Nature*, 458(7236), 322–328. <https://doi.org/10.1038/nature07867>
- 1064 Nickel, K. G., & Green, D. H. (1985). Empirical geothermobarometry for garnet peridotites and
1065 implications for the nature of the lithosphere, kimberlites and diamonds. *Earth and*
1066 *Planetary Science Letters*, 73(1), 158–170. [https://doi.org/10.1016/0012-821X\(85\)90043-3](https://doi.org/10.1016/0012-821X(85)90043-3)
- 1067 Pagani, M., Liu, Z., LaRiviere, J., & Ravelo, A. C. (2010). High Earth-system climate sensitivity
1068 determined from Pliocene carbon dioxide concentrations. *Nature Geoscience*, 3(1), 27–
1069 30. <https://doi.org/10.1038/ngeo724>
- 1070 Pedoja, K., Regard, V., Husson, L., Martinod, J., Guillaume, B., Fucks, E., Iglesias, M., & Weill, P.
1071 (2011). Uplift of quaternary shorelines in eastern Patagonia: Darwin revisited.
1072 *Geomorphology*, 127(3), 121–142. <https://doi.org/10.1016/j.geomorph.2010.08.003>
- 1073 Peltier, W. R., Argus, D. F., & Drummond, R. (2015). Space geodesy constrains ice age terminal
1074 deglaciation: The global ICE-6G_C (VM5a) model. *Journal of Geophysical Research: Solid*
1075 *Earth*, 120(1), 450–487. <https://doi.org/10.1002/2014JB011176>
- 1076 Peltier, W. R., & Fairbanks, R. G. (2006). Global glacial ice volume and Last Glacial Maximum
1077 duration from an extended Barbados sea level record. *Quaternary Science Reviews*,
1078 25(23), 3322–3337. <https://doi.org/10.1016/j.quascirev.2006.04.010>
- 1079 Perucca, L., Alvarado, P., & Saez, M. (2016). Neotectonics and seismicity in southern Patagonia.
1080 *Geological Journal*, 51(4), 545–559. <https://doi.org/10.1002/gj.2649>
- 1081 Pollard, D., DeConto, R. M., & Alley, R. B. (2015). Potential Antarctic Ice Sheet retreat driven by
1082 hydrofracturing and ice cliff failure. *Earth and Planetary Science Letters*, 412, 112–121.
1083 <https://doi.org/10.1016/j.epsl.2014.12.035>
- 1084 Raymo, M. E., Kozdon, R., Evans, D., Lisiecki, L., & Ford, H. L. (2018). The accuracy of mid-
1085 Pliocene $\delta^{18}\text{O}$ -based ice volume and sea level reconstructions. *Earth-Science Reviews*,
1086 177, 291–302. <https://doi.org/10.1016/j.earscirev.2017.11.022>
- 1087 Raymo, M. E., Mitrovica, J. X., O’Leary, M. J., DeConto, R. M., & Hearty, P. J. (2011). Departures
1088 from eustasy in Pliocene sea-level records. *Nature Geoscience*, 4(5), 328–332.
1089 <https://doi.org/10.1038/ngeo1118>
- 1090 Richards, F. D., Hoggard, M. J., White, N., & Ghelichkhan, S. (2020). Quantifying the Relationship
1091 Between Short-Wavelength Dynamic Topography and Thermomechanical Structure of
1092 the Upper Mantle Using Calibrated Parameterization of Anelasticity. *Journal of*
1093 *Geophysical Research: Solid Earth*, 125(9), e2019JB019062.
1094 <https://doi.org/10.1029/2019JB019062>
- 1095 Richards, F., Hoggard, M. J., Ghelichkhan, S., Koelemeijer, P., & Lau, H. (2021). *Geodynamic,*
1096 *geodetic, and seismic constraints favour deflated and dense-cored LLVPs.*
1097 <https://eartharxiv.org/repository/view/2465/>
- 1098 Ritsema, J., Deuss, A., van Heijst, H. J., & Woodhouse, J. H. (2011). S40RTS: A degree-40 shear-
1099 velocity model for the mantle from new Rayleigh wave dispersion, teleseismic travelttime
1100 and normal-mode splitting function measurements. *Geophysical Journal International*,
1101 184(3), 1223–1236. <https://doi.org/10.1111/j.1365-246X.2010.04884.x>
- 1102 Rohling, E. J., Foster, G. L., Grant, K. M., Marino, G., Roberts, A. P., Tamisiea, M. E., & Williams, F.
1103 (2014). Sea-level and deep-sea-temperature variability over the past 5.3 million years.
1104 *Nature*, 508(7497), 477–482. <https://doi.org/10.1038/nature13230>
- 1105

- 1106 Rovere, A., Pappalardo, M., Richiano, S., Aguirre, M., Sandstrom, M. R., Hearty, P. J., Austermann,
1107 J., Castellanos, I., & Raymo, M. E. (2020). Higher than present global mean sea level
1108 recorded by an Early Pliocene intertidal unit in Patagonia (Argentina). *Communications
1109 Earth & Environment*, 1(1), 1–10. <https://doi.org/10.1038/s43247-020-00067-6>
- 1110 Rovere, A., Raymo, M. E., Mitrovica, J. X., Hearty, P. J., O’Leary, M. J., & Inglis, J. D. (2014). The
1111 Mid-Pliocene sea-level conundrum: Glacial isostasy, eustasy and dynamic topography.
1112 *Earth and Planetary Science Letters*, 387, 27–33.
1113 <https://doi.org/10.1016/j.epsl.2013.10.030>
- 1114 Rowley, D. B., Forte, A. M., Mouche, R., Mitrovica, J. X., Simmons, N. A., & Grand, S. P. (2013).
1115 Dynamic Topography Change of the Eastern United States Since 3 Million Years Ago.
1116 *Science*, 340(6140), 1560–1563. <https://doi.org/10.1126/science.1229180>
- 1117 Russo, R. M., Luo, H., Wang, K., Ambrosius, B., Mocanu, V., He, J., James, T., Bevis, M., &
1118 Fernandes, R. (2022). Lateral variation in slab window viscosity inferred from global
1119 navigation satellite system (GNSS)–observed uplift due to recent mass loss at Patagonia
1120 ice fields. *Geology*, 50(1), 111–115. <https://doi.org/10.1130/G49388.1>
- 1121 Schaeffer, A. J., & Lebedev, S. (2013). Global shear speed structure of the upper mantle and
1122 transition zone. *Geophysical Journal International*, 194(1), 417–449.
1123 <https://doi.org/10.1093/gji/ggt095>
- 1124 Scherer, R. P., DeConto, R. M., Pollard, D., & Alley, R. B. (2016). Windblown Pliocene diatoms and
1125 East Antarctic Ice Sheet retreat. *Nature Communications*, 7(1), 12957.
1126 <https://doi.org/10.1038/ncomms12957>
- 1127 Seki, O., Foster, G. L., Schmidt, D. N., Mackensen, A., Kawamura, K., & Pancost, R. D. (2010).
1128 Alkenone and boron-based Pliocene pCO₂ records. *Earth and Planetary Science Letters*,
1129 292(1), 201–211. <https://doi.org/10.1016/j.epsl.2010.01.037>
- 1130 Steinberger, B. (2016a). Topography caused by mantle density variations: Observation-based
1131 estimates and models derived from tomography and lithosphere thickness. *Geophysical
1132 Journal International*, 205(1), 604–621. <https://doi.org/10.1093/gji/ggw040>
- 1133 Steinberger, B. (2016b). Topography caused by mantle density variations: Observation-based
1134 estimates and models derived from tomography and lithosphere thickness. *Geophysical
1135 Journal International*, 205(1), 604–621. <https://doi.org/10.1093/gji/ggw040>
- 1136 Tackley, P. J., Stevenson, D. J., Glatzmaier, G. A., & Schubert, G. (1994). Effects of multiple phase
1137 transitions in a three-dimensional spherical model of convection in Earth’s mantle.
1138 *Journal of Geophysical Research: Solid Earth*, 99(B8), 15877–15901.
1139 <https://doi.org/10.1029/94JB00853>
- 1140 Taylor, W. R. (1998). An experimental test of some geothermometer and geobarometer
1141 formulations for upper mantle peridotites with application to the thermobarometry of
1142 fertile lherzolite and garnet websterite. *Neues Jahrbuch Für Mineralogie - Abhandlungen*,
1143 381–408. <https://doi.org/10.1127/njma/172/1998/381>
- 1144 Thorkelson, D. J., Madsen, J. K., & Sluggett, C. L. (2011). Mantle flow through the Northern
1145 Cordilleran slab window revealed by volcanic geochemistry. *Geology*, 39(3), 267–270.
1146 <https://doi.org/10.1130/G31522.1>
- 1147 Waelbroeck, C., Labeyrie, L., Michel, E., Duplessy, J. C., McManus, J. F., Lambeck, K., Balbon, E., &
1148 Labracherie, M. (2002). Sea-level and deep water temperature changes derived from

- 1149 benthic foraminifera isotopic records. *Quaternary Science Reviews*, 21(1), 295–305.
1150 [https://doi.org/10.1016/S0277-3791\(01\)00101-9](https://doi.org/10.1016/S0277-3791(01)00101-9)
- 1151 Wang, J., Hattori, K. H., Li, J., & Stern, C. R. (2008). Oxidation state of Paleozoic subcontinental
1152 lithospheric mantle below the Pali Aike volcanic field in southernmost Patagonia. *Lithos*,
1153 105(1), 98–110. <https://doi.org/10.1016/j.lithos.2008.02.009>
- 1154 Wiens, D., Mansour, W. B., Mark, H. F., Shore, P., Richter, A., & Barrientos, S. E. (2021, December
1155 17). *Geodynamics of the Patagonian Slab Window Constrained by Shear Wave Splitting
1156 and Seismic Imaging*. AGU Fall Meeting 2021.
1157 <https://agu.confex.com/agu/fm21/meetingapp.cgi/Paper/975656>
- 1158 Wolfgang Bangerth, Juliane Dannberg, Rene Gassmoeller, & Timo Heister. (2020). ASPECT v2.2.0.
1159 Zenodo. <https://doi.org/10.5281/zenodo.3924604>
- 1160 Yamauchi, H., & Takei, Y. (2016). Polycrystal anelasticity at near-solidus temperatures. *Journal of
1161 Geophysical Research: Solid Earth*, 121(11), 7790–7820.
1162 <https://doi.org/10.1002/2016JB013316>
- 1163 Zheng, L., Gordon, R. G., & Kreemer, C. (2014). Absolute plate velocities from seismic anisotropy:
1164 Importance of correlated errors. *Journal of Geophysical Research: Solid Earth*, 119(9),
1165 7336–7352. <https://doi.org/10.1002/2013JB010902>
- 1166 Zhong, S., Gurnis, M., & Hulbert, G. (1993). Accurate determination of surface normal stress in
1167 viscous flow from a consistent boundary flux method. *Physics of the Earth and Planetary
1168 Interiors*, 78(1), 1–8. [https://doi.org/10.1016/0031-9201\(93\)90078-N](https://doi.org/10.1016/0031-9201(93)90078-N)
- 1169
- 1170